U.S. Department of the Interior
U.S. Geological Survey

Prepared for the
National Aeronautics and Space Administration

Scientific Investigations Map 2898
Atlas of Venus: Sif Mons Quadrangle (V–31)

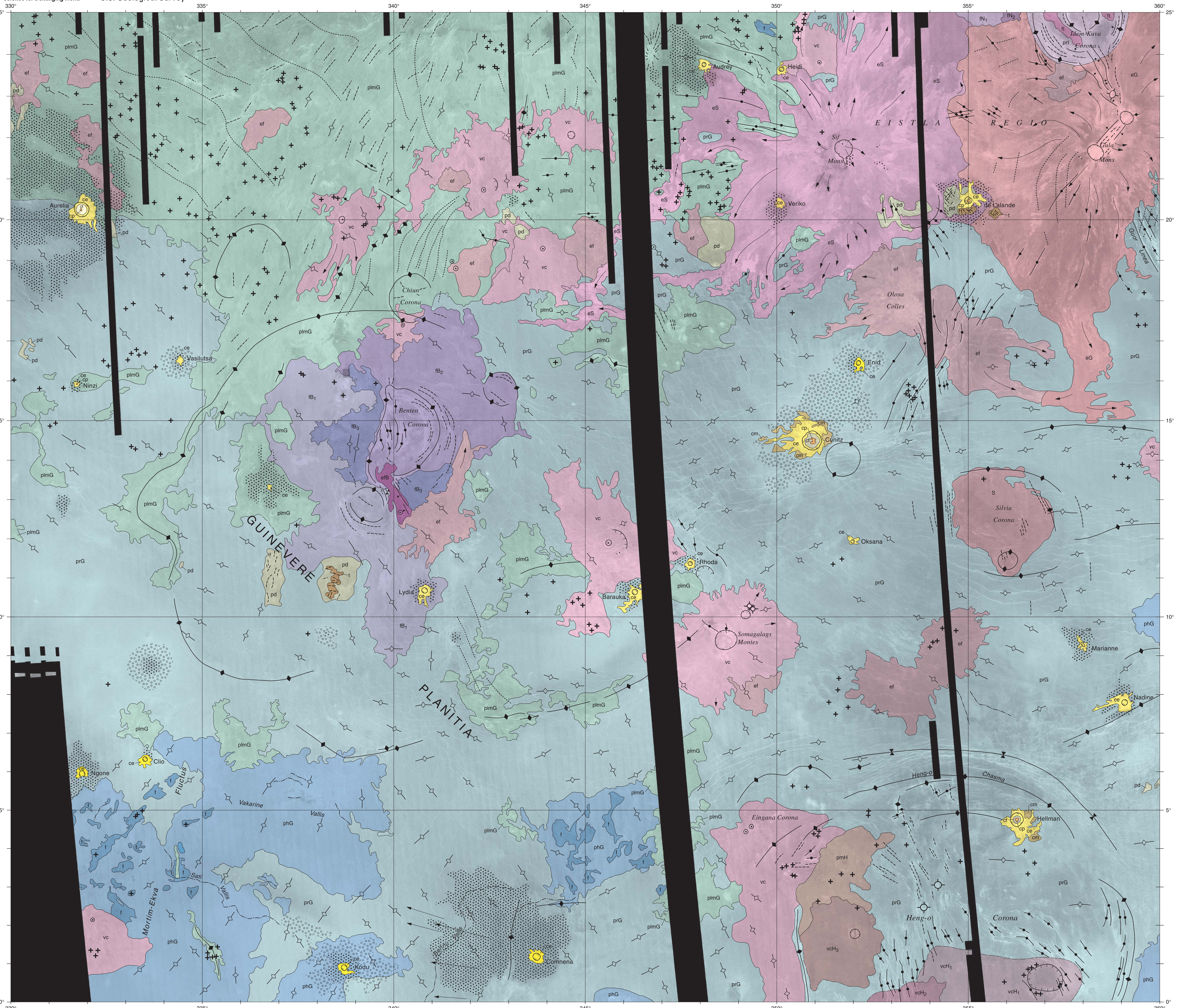

Descriptions of nomenclature used on map are listed at http://planetarynames.wr.usgs.gov/

SCALE 1:5 198 991 (1 mm = 5.199 km) AT 0° LATITUDE
1:4 711 886 AT 25° LATITUDE
MERCATOR PROJECTION

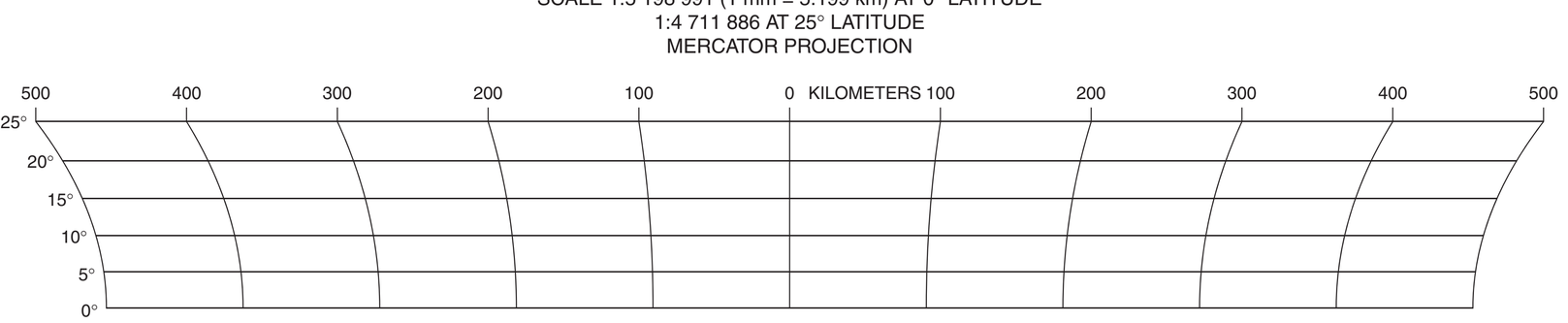

Prepared on behalf of the Planetary Geology and Geophysics Program, Solar System Exploration Division, Office of Space Science, National Aeronautics and Space Administration
Edited by Jan L. Zigler
Cartography by Darlene A. Ryan
Manuscript approved for publication September 12, 2005

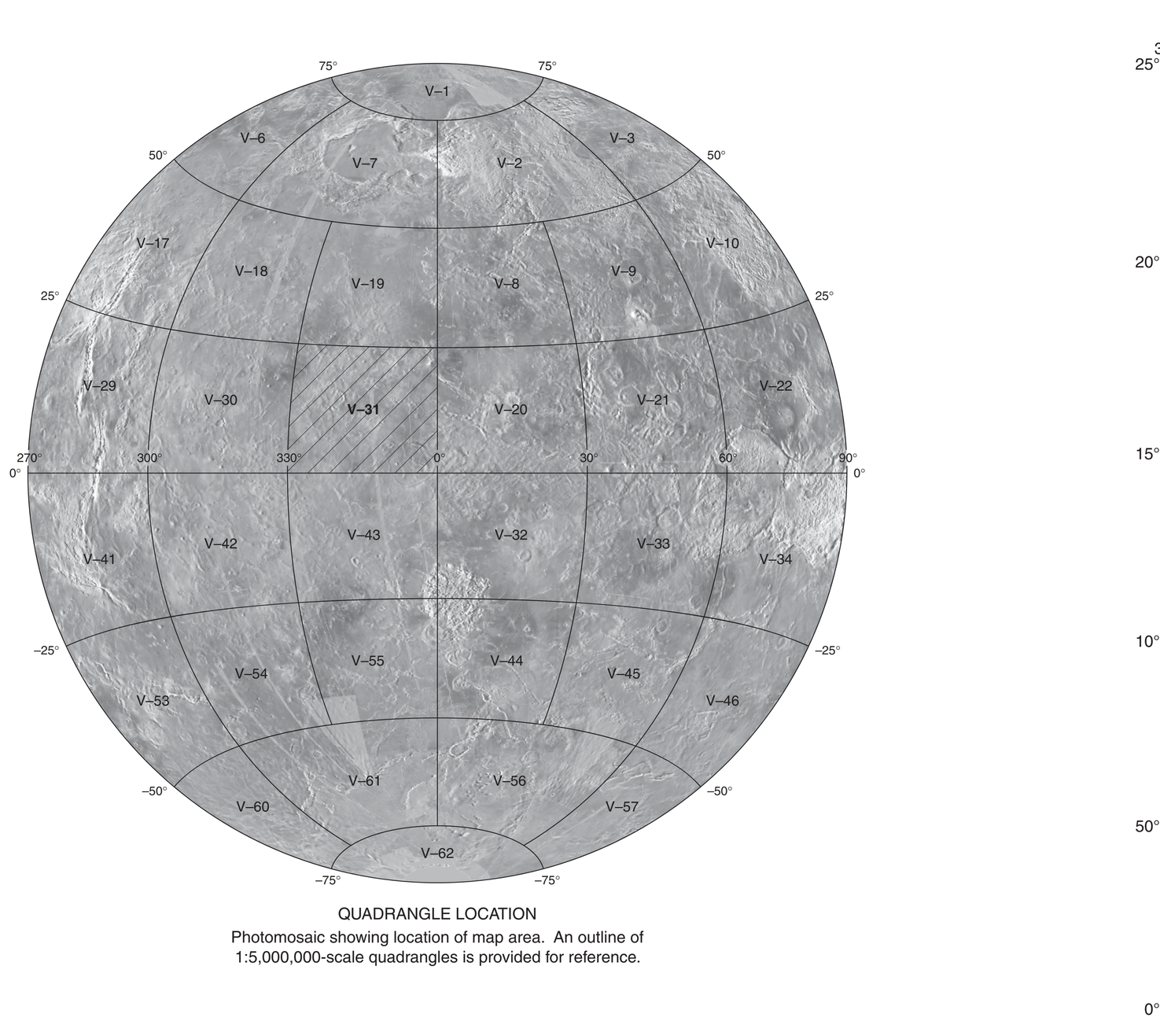

QUADRANGLE LOCATION
Photomosaic showing location of map area. An outline of 1:5,000,000-scale quadrangles is provided for reference.

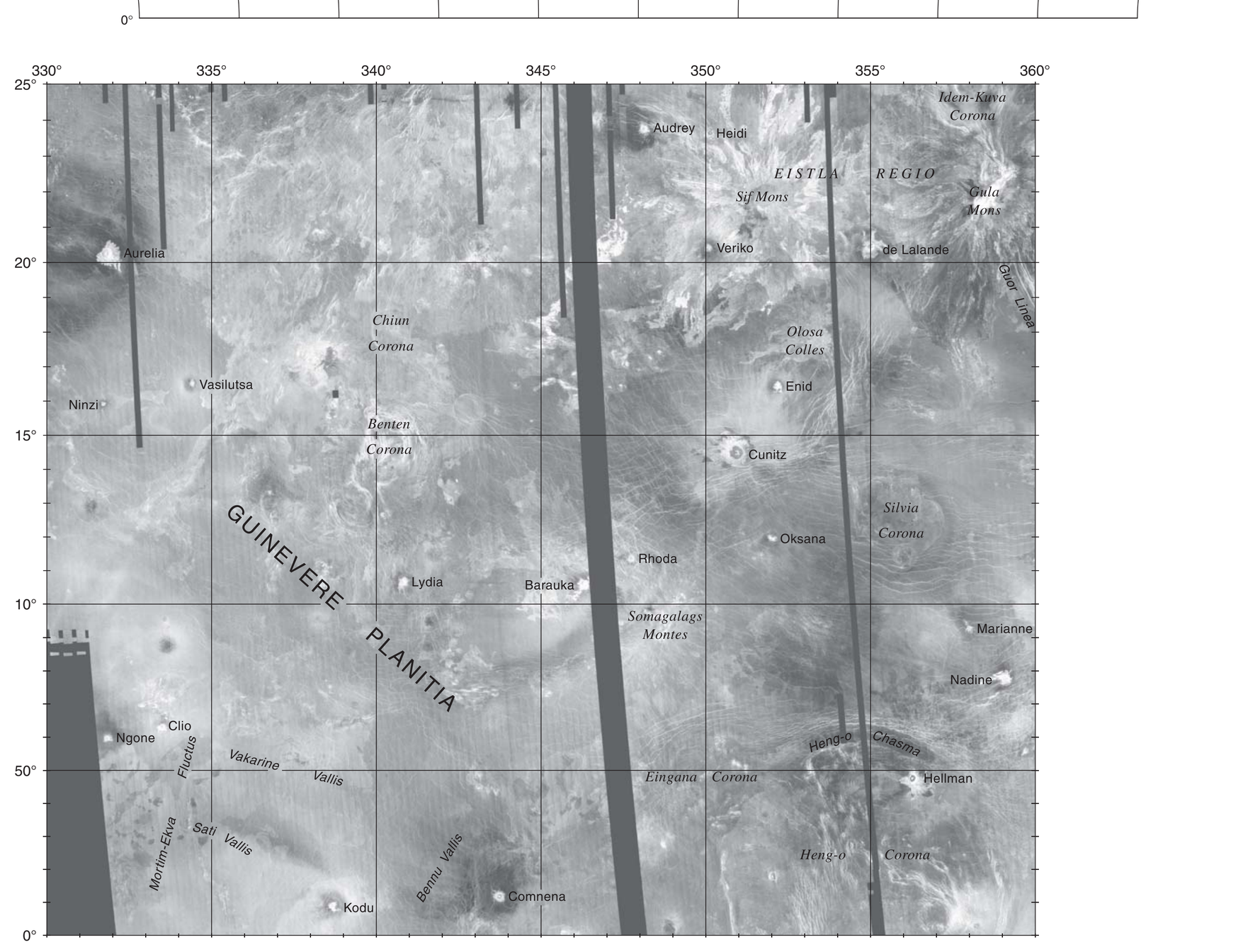

Figure 1. Synthetic aperture radar (SAR) backscatter mosaic of Sif Mons quadrangle (V–31), Venus, showing major features.

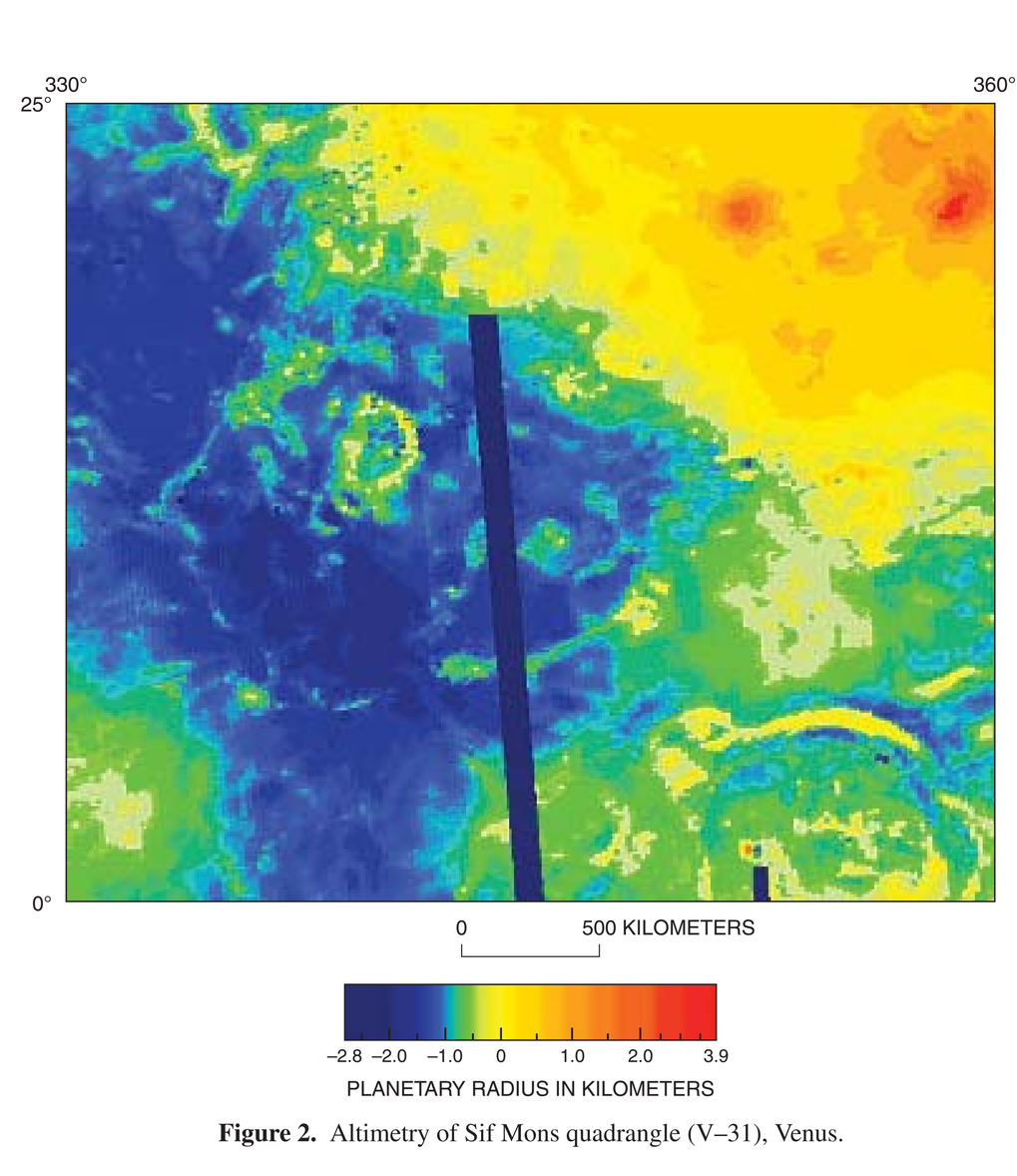

Figure 2. Altimetry of Sif Mons quadrangle (V–31), Venus.

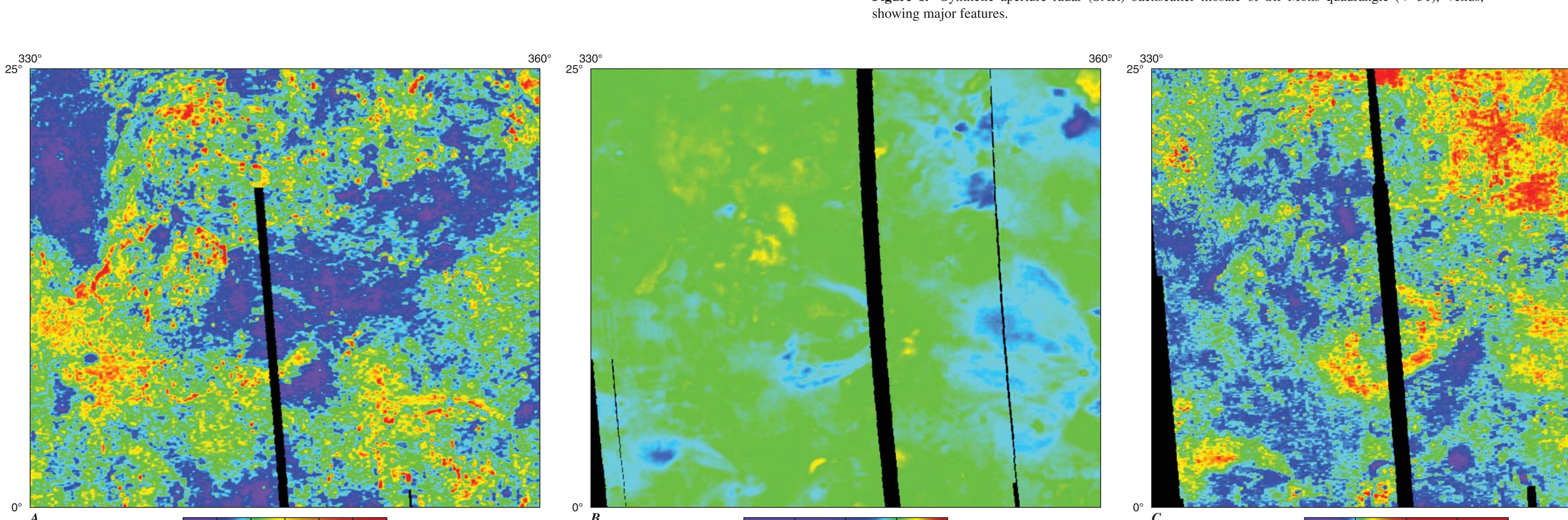

Figure 3. Images of ancillary data for Sif Mons quadrangle (V–31), Venus. ***A***, rms slope data; ***B***, emissivity data; ***C***, reflectivity data.

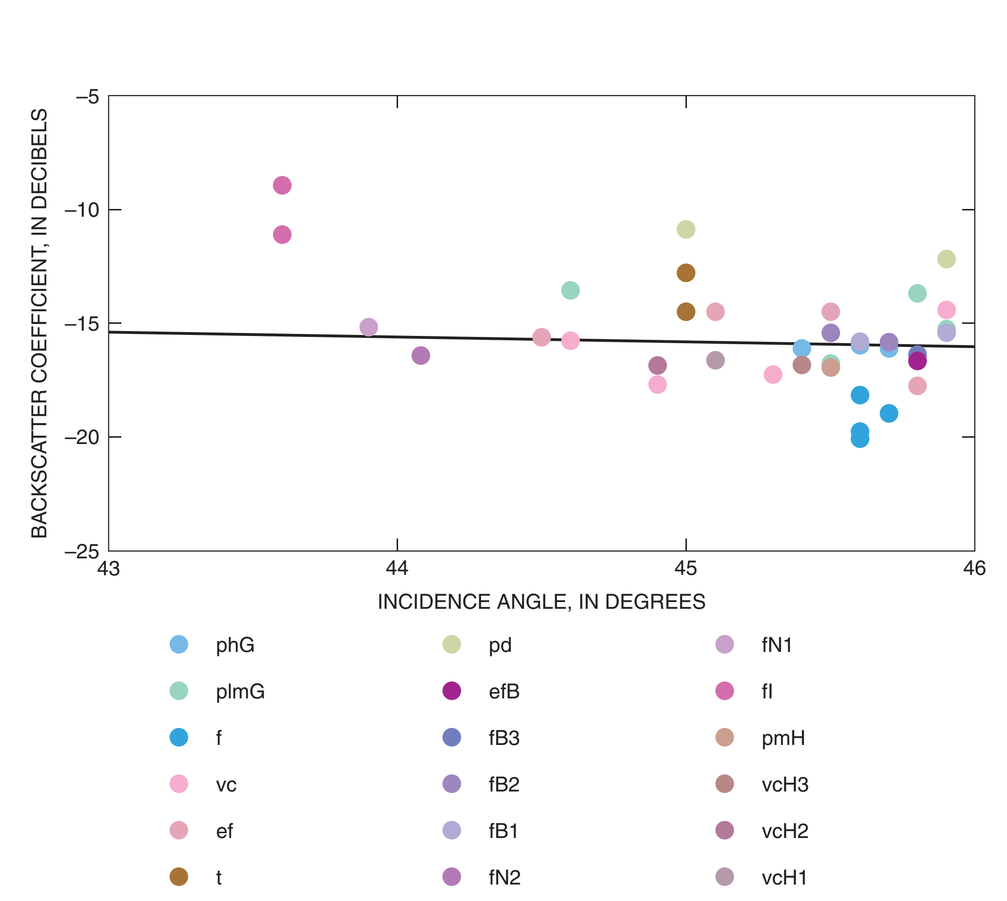

Figure 4. Backscatter coefficient (σ_0) for selected units in Sif Mons quadrangle (V–31), Venus. Line represents mean backscatter for Venus.

Geologic Map of the Sif Mons Quadrangle (V–31), Venus

By

Duncan L. Copp[1] and John E. Guest[1]

2007

[1]University College, London, UK

CORRELATION OF MAP UNITS

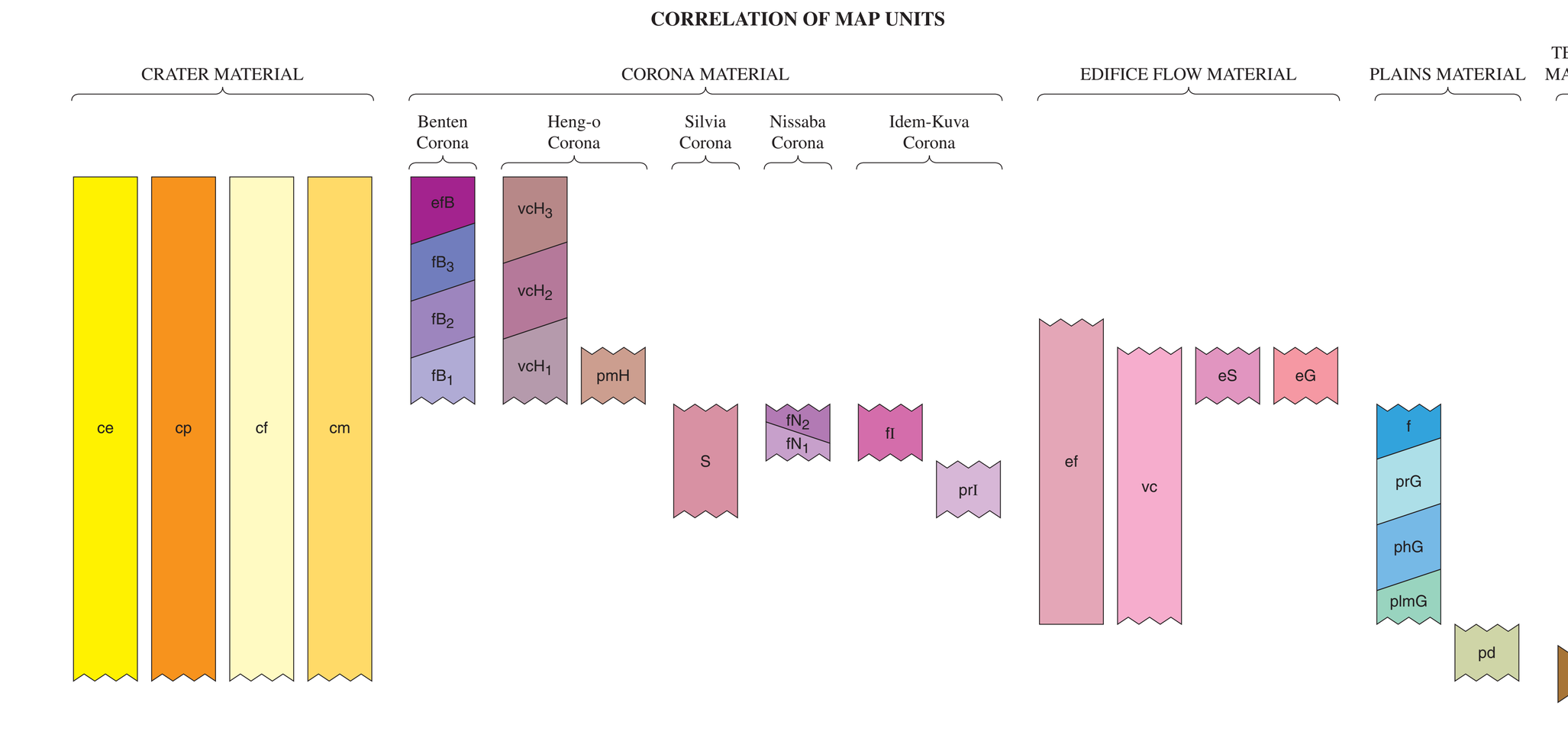

DESCRIPTION OF MAP UNITS

CRATER MATERIAL

ce **Crater ejecta material**—Has high-radar-backscatter coefficient and surrounds craters. Has lobate, gradational distal boundaries. Material may be markedly asymmetrical. Postdates plains materials and, locally, is typically the youngest unit. *Type locality*: lat 14.7° N., long 350.7° E. *Interpretation*: Ejecta excavated by impact cratering. Asymmetrical ejecta provides an indication of entry direction of meteoroid

cp **Crater peak material**—Forms single or multiple peaks on crater floor; embayed by unit cf. Has high-radar-backscatter coefficient. Only mapped in craters with diameters >35 km. *Type locality*: lat 14.46° N., long 350.97° E. *Interpretation*: Material deformed and uplifted from beneath crater floor during late-stage crater excavation

cf **Crater floor material**—Low-radar-backscatter coefficient material within interior floors of larger craters. Embays both crater walls and unit cp where present. Small wrinkle ridges are observed in some craters. Unit cf is mapped in craters with diameters >35 km. *Type locality*: lat 14.4° N., long 350.8° E. *Interpretation*: Relatively smooth material; either impact melt, volcanic lava, or both

cm **Crater margin material**—Has low-radar-backscatter coefficient; sharp proximal boundaries may fade distally and are often topographically controlled. Superposed on plains units but truncated by crater ejecta. *Type locality*: lat 4.9° N., long 351.2° E. *Interpretation*: Smooth deposits produced by atmospheric and ground shockwave interaction producing comminuted material

CORONA MATERIAL

Benten Corona

efB **Benten Corona edifice field material**—Forms irregular field of small edifices in interior of Benten Corona. Unit postdates fB_3 material. *Type locality*: lat 12.5° N., long 340.7° E. *Interpretation*: Late-stage volcanism associated with Benten Corona

fB_3 **Benten Corona flow material 3**—Material that has a flow-like form associated with Benten Corona. Radar backscatter coefficient changes with distance from corona. Represents the youngest flow apron of corona. *Type locality*: lat 15° N., long 339° E. *Interpretation*: Lava flows associated with late-stage activity of Benten Corona

fB_2 **Benten Corona flow material 2**—Consists of compound flows that display a variable radar backscatter coefficient. Flow boundaries have a more lobate morphology than fB_3 and are clearly deformed by the north and northeast annulus of Benten Corona. Superposed on units prG, plmG, and fB_1; embayed by unit fB_3. *Type locality*: lat 16.5° N., long 341° E. *Interpretation*: Product of effusive volcanism associated with Benten Corona

fB_1 **Benten Corona flow material 1**—Generally has a homogeneous-radar-backscatter coefficient. Few individual flows can be identified within unit. *Type locality*: lat 15.7° N., long 337.5° E. *Interpretation*: Early stage effusive volcanism from Benten Corona

Heng-o Corona

vcH_3 **Heng-o Corona volcanic center material 3**—Has a moderate-radar-backscatter coefficient associated with a prominent edifice located at lat 1.78° N., long 352.01° E. Unit postdates unit pmH and is contained by western annulus of Heng-o Corona. *Type locality*: lat 2.43° N., long 351.80° E. *Interpretation*: Late stage lava flows that postdate the large-scale deformation of Heng-o Corona

vcH_2 **Heng-o Corona volcanic center material 2**—Has a moderate-radar-backscatter coefficient associated with prominent edifice located at lat −0.62° N., long 353.22° E., south of V–31. The edifice is cut by north-northwest-trending fractures that are embayed by unit vcH_3. *Type locality*: lat 0.25° N., long 354° E. *Interpretation*: Volcano with radiating lava flow field

vcH_1 **Heng-o Corona volcanic center material 1**—Has a moderate but variable radar backscatter coefficient associated with a large edifice approximately 50 km in diameter centered at lat 0.62° N., long 356.97° E. The summit of the edifice is circled by many smaller edifices and is cut by northwest-trending fractures. The unit is superposed by vcH_2 material and is deformed by structures within the eastern sector of Heng-o. *Type locality*: lat 0.5° N., long 356° E. *Interpretation*: Lava flows associated with a volcanic center, the summit of which has ring fractures and small volcanic shields

pmH **Heng-o Corona mottled plains material**—Has a variable backscatter coefficient similar to unit plmG. Unit is moderately deformed and contains small edifices. *Type locality*: lat 3° N., long 353° E. The unit predates units vc and vcH_3 associated with Heng-o Corona and is cut by interior deformation associated with Heng-o Corona. *Interpretation*: Volcanic materials that have been deformed by later structures associated with the formation of Heng-o Corona

Silvia Corona

S **Silvia Corona material**—High-standing material with mottled-intermediate-radar-backscatter coefficients. Has undergone greater deformation than the surrounding plains, unit prG, by which it is embayed. Contains a number of small edifices. *Type locality*: lat 12.5° N., long 356° E. *Interpretation*: Earlier volcanic plains material uplifted and deformed during the formation of Silvia Corona

Nissaba Corona

fN_2 **Nissaba Corona flow material 2**—Exhibits a low-radar-backscatter coefficient; associated with a small edifice situated on rim of corona. Unit fN_2 postdates fN_1. *Type locality*: lat 24.9° N., long 356° E. *Interpretation*: Lava flow erupted from a small volcano associated with the formation of Nissaba Corona

fN_1 **Nissaba Corona flow material 1**—Has digitate morphology and variable radar backscatter coefficients. Unit fN_1 postdates structures associated with the formation of Nissaba Corona. *Type locality*: lat 24.8° N., long 355.5° E. *Interpretation*: Lavas associated with the formation of Nissaba Corona

Idem-Kuva Corona

fI **Idem-Kuva Corona flow material**—Has high-radar-backscatter coefficient and is typified by digitate boundary. Unit postdates prI. *Type locality*: lat 29.5° N., long 357.2° E. *Interpretation*: Late-stage flows that formed after the corona annulus

prI **Idem-Kuva Corona relic plains material**—Plains material with moderate-radar-backscatter coefficients similar to unit phG. Unit is moderately to severely deformed by compressional and extensional fractures. Unit is superposed by unit fI. *Type locality*: lat 25.8° N., long 358° E. *Interpretation*: Earlier volcanic plains material having undergone uplift and deformation during the formation of Idem-Kuva Corona

EDIFICE FLOW MATERIAL

ef **Edifice field material**—Characterized by a concentration of small (normally <10 km diameter) hills of variable morphology but dominantly with a low profile. Some edifice fields have associated compound flow aprons. Unit has a variable stratigraphic range. *Type locality*: lat 18° N., long 342° E. *Interpretation*: Volcanic complex of small volcanoes, probably associated with a long-lived shallow magma reservoir

vc **Volcanic center material**—Makes up intermediate-sized edifices >15 km diameter. Has variable radar backscatter coefficients. Boundaries are often diffuse and (or) lobate. The unit postdates prG and phG. *Type locality*: lat 19° N., long 344° E. *Interpretation*: Volcanic centers of either monogenetic or polygenetic origin with associated lava flows

eS **Sif Mons material**—Material with a flow-like form associated with Sif Mons. Individual flows have different morphologies, and radar backscatter coefficients vary from flow to flow and within flow units. Superposed on units prG and plmG. *Type locality*: lat 20° N., long 351.7° E. *Interpretation*: Lava flows erupted from the Sif Mons volcano

eG **Gula Mons material**—Material with a flow-like form associated with large edifice Gula Mons. Individual flows have different morphologies, predominantly digitate. Radar backscatter coefficients vary from flow to flow and within flow units. Individual units often have distinct lobate boundaries. Superposes all plains units, excluding f. *Type locality*: lat 20° N., long 358° E. *Interpretation*: Lava flows associated with the Gula Mons volcano

PLAINS MATERIAL

f **Isolated flow material**—Small irregular outcrops characterized by relatively low-radar-backscatter coefficients. Digitate to lobate boundaries that are often topographically controlled. Small pits are frequent. Some outcrops appear to have been modified by surficial crater material. Superposed on all plains units. *Type locality*: lat 4.8° N., long 335.2° E. *Interpretation*: Lava flows; small pits represent vents

prG **Guinevere Planitia regional plains material**—Extensive unit has a comparatively low radar backscatter coefficient that is generally homogeneous but, in places, patchy. Has a fabric of wrinkle ridges of varying orientation, although the dominant trend is northwest-southeast. A local reticulate pattern of wrinkle ridges occurs in places. Small volcanic edifices are identified that have a similar radar backscatter to surrounding plains. Embays phG but is superposed by eG, eS, and some ef material. *Type locality*: lat 17.94° N., long 333.28° E. *Interpretation*: Extensive lava plains with relatively smooth surfaces deformed by compressional stresses

phG **Guinevere Planitia homogeneous plains material**—Has a medium radar backscatter coefficient, giving a homogeneous appearance. Deficient in small edifices. Contains numerous wrinkle ridges. The boundaries of the unit are often diffuse and sometimes difficult to identify precisely. Embayed by unit prG. *Type locality*: lat 1° N., long 335° E. *Interpretation*: Volcanic material (lava flows) with a rough surface texture at centimeter scale deformed by compressional stresses

plmG **Guinevere Planitia lineated and mottled plains material**—Radar backscatter coefficient variable. Contains abundant edifices typically 2–5 km in diameter and predominantly of a shield morphology. The unit has a greater elevation than unit prG. Displays numerous styles of deformation (ridges, grabens, and fractures). A fine polygonal fabric is common. Embayed by units prG and phG. *Type locality*: lat 21.94° N., long 337.8° E. *Interpretation*: Numerous small volcanic edifices and associated flows forming volcanic plains cut by ridges and grabens

pd **Deformed plains material**—Small inliers of plains material that are cut by fractures. Has high-radar-backscatter coefficient. Embayed by units prG and plmG. *Type locality*: lat 11.25° N., long 336.5° E. *Interpretation*: Lava that has been tectonically modified

TESSERA MATERIAL

t **Tessera material**—Inlier of upstanding material with a high-radar-backscatter coefficient. Contains numerous closely spaced fractures oriented in more than one direction. *Type locality*: lat 20° N., long 335° E. *Interpretation*: Highly deformed material that may represent older deformed plains material or an early crust of different composition from the surrounding plains material

Contact—Dashed where approximately located or arbitrarily located based on edifice densities. Internal contact separates volcanic centers

Wrinkle ridge—Compressional deformation analogous to Lunar and Martian wrinkle ridges

Lineament

Curvilinear lineament—Surface manifestation of subsurface dikes

Ridge—Large-scale topographic features commonly associated with coronae. Barbs point downslope from ridge crest

Trough—Large-scale topographic features commonly associated with coronae. Barbs point downslope towards trough

Graben—Bar and ball on downthrown sides of widely separated boundary faults; ball on line where boundary faults closely spaced

Scarp—Line marks top of slope; hachures point downslope

Channel, narrow and sinuous—Formed by lava erosion

Volcanic edifice (<15 km diameter)

Volcanic edifice (>15 km diameter)

Volcanic dome (5–40 km diameter)

Inferred flow direction of flow lobe

Caldera or depression—Volcanic in origin. Formed by collapse

Impact crater rim

Superficial crater material—High-radar-backscatter coefficient

Superficial crater material—Low-radar-backscatter coefficient

Table 1. *Location data for ancillary radar samples of selected units within the Sif Mons quadrangle (V–31), Venus*

[Units that have numerous outcrops or have large surface area were sampled more than once in a widely spaced area]

Unit label	Sample area latitude (° N.)	Sample area longitude (° E.)	Pixel scale, Δ (m)	No. of pixels, *N*	Incidence angle, ι (deg)	Radius (km) (min., max.)
prG	14.290, 15.190	347.340, 348.190	205,530	225	45.7	6,050.766 (6,050.630, 6,051.022)
prG	16.240, 17.120	342.300, 343.360	192,750	225	45.5	6,050.569 (6,050.325, 6,050.769)
prG	7.200, 8.110	339.560, 341.700	223,512	225	45.9	6,050.218 (6,050.001, 6,050.541)
prG	16.040, 16.550	330.540, 332.100	225,834	225	45.5	6,050.493 (6,050.349, 6,050.696)
phG	1.490, 2.420	333.200, 334.310	231,712	225	45.4	6,051.093 (6,051.017, 6,051.192)
phG	3.500, 4.400	334.460, 335.410	170,640	225	45.6	6,050.982 (6,050.771, 6,051.223)
phG	3.490, 4.160	345.130, 345.400	44,099	225	45.6	6,051.288 (6,051.120, 6,051.415)
phG	4.560, 5.200	345.120, 345.340	32,448	225	45.7	6,050.904 (6,050.729, 6,051.068)
plmG	21.150, 22.010	339.180, 340.220	172,674	225	44.6	6,051.300 (6,050.564, 6,051.659)
plmG	12.310, 13.220	333.080, 333.480	125,955	225	45.8	6,050.798 (6,049.867, 6,051.009)
plmG	16.390, 17.090	345.340, 346.050	54,747	225	45.5	6,051.185 (6,050.745, 6,051.587)
plmG	11.070, 11.420	342.520, 343.570	134,534	225	45.9	6,050.818 (6,050.513, 6,051.148)
f	4.500, 4.560	335.040, 335.120	3,100	225	45.7	6,050.911 (6,050.909, 6,050.915)
f	4.010, 4.050	333.170, 333.230	1,734	225	45.6	6,051.255 (6,051.238, 6,051.273)
f	3.350, 3.420	346.200, 346.430	8,083	225	45.6	6,051.204 (6,051.185, 6,051.215)
f	4.070, 4.200	344.140, 344.280	11,000	225	45.6	6,050.982 (6,050.970, 6,051.010)
vc	7.560, 8.420	347.480, 348.500	199,892	225	45.9	6,050.985 (6,050.774, 6,051.286)
vc	21.430, 22.140	344.470, 345.160	54,312	225	44.6	6,051.948 (6,051.591, 6,052.641)
vc	19.420, 20.250	339.110, 339.260	40,560	225	44.9	6,051.236 (6,050.927, 6,051.451)
vc	1.240, 2.090	332.210, 332.520	88,250	225	45.3	6,051.329 (6,051.243, 6,051.564)
ef	17.330, 18.110	353.010, 353.360	79,864	225	45.4	6,052.618 (6,052.382, 6,052.755)
ef	12.120, 12.470	340.380, 341.120	76,713	225	45.8	6,050.877 (6,050.708, 6,051.120)
ef	21.580, 22.250	336.220, 336.520	45,333	225	44.5	6,050.779 (6,050.712, 6,050.865)
ef	18.400, 19.140	341.520, 342.290	77,452	225	45.1	6,050.970 (6,050.722, 6,051.342)
t	20.090, 20.150	354.560, 355.070	4,150	225	45.0	6,052.997 (6,052.806, 6,053.151)
t	20.060, 20.130	355.410, 355.480	2,900	225	45.0	6,052.633 (6,052.622, 6,052.649)
pd	19.380, 19.500	343.140, 343.240	7,296	225	45.0	6,051.412 (6,051.356, 6,051.462)
pd	10.390, 10.500	338.170, 338.300	7,938	225	45.9	6,050.584 (6,050.422, 6,050.722)
efB	13.270, 13.380	339.330, 339.550	14,705	225	45.8	6,051.291 (6,051.154, 6,051.338)
fB_3	13.180, 13.510	340.460, 341.140	59,701	225	45.8	6,051.139 (6,050.622, 6,051.485)
fB_3	14.090, 14.570	338.330, 339.010	83,276	225	45.7	6,050.880 (6,050.541, 6,051.389)
fB_2	14.430, 15.340	341.470, 342.310	140,298	225	45.7	6,050.528 (6,049.918, 6,050.938)
fB_2	16.220, 17.040	340.370, 341.200	110,544	225	45.5	6,050.637 (6,050.414, 6,050.917)
fB_1	15.240, 16.010	337.310, 338.130	95,016	225	45.6	6,050.721 (6,050.616, 6,050.943)
fB_1	11.020, 11.370	339.590, 340.220	49,775	225	45.9	6,050.340 (6,050.129, 6,050.562)
fN_2	24.490, 24.590	355.560, 356.040	4,880	225	43.9	6,052.529 (6,052.454, 6,052.639)
fN_1	24.540, 25.010	355.110, 355.420	13,320	225	43.9	6,051.842 (6,050.704, 6,052.059)
fI	26.010, 26.160	358.290, 358.430	8,840	225	43.6	6,052.416 (6,052.387, 6,052.442)
fI	25.400, 25.530	357.000, 357.110	13,750	225	43.6	6,052.475 (6,052.438, 6,052.511)
pmH	2.500, 3.060	350.500, 351.350	45,234	225	45.5	6,051.106 (6,051.000, 6,051.431)
vcH_1	0.050, 0.430	355.330, 355.530	58,435	225	45.1	6,051.396 (6,051.275, 6,051.485)
vcH_2	−1.040, 0.380	352.160, 352.560	65,508	225	44.9	6,051.339 (6,051.305, 6,051.375)
vcH_3	2.070, 2.220	350.390, 351.360	53,788	225	45.4	6,051.078 (6,051.018, 6,051.261)

Table 2. *Ancillary radar data for sampled areas within the Sif Mons quadrangle (V–31), Venus*

[For the backscatter coefficient, values in parentheses represent the σ_0 value (in dB) at ±1 standard deviation; all other data in parentheses represent minimum and maximum values for the selected sample area. Dielectric constants are for smooth surfaces (ε_s) and rough surfaces (ε_r). Units that are numerous or have a large surface area were sampled more than once in widely spaced areas]

Unit label	Backscatter, σ_0 (dB)	Root-mean-square slope, θ_{rms} (deg)	Fresnel reflectivity, ρ	Emissivity	Dielectric constant ε_s, ε_r
prG	−19.34 (−26.03, −20.04)	1.78 (1.10, 2.40)	0.103 (0.080, 0.130)	0.832 (0.825, 0.839)	3.3, 5.4
prG	−17.89 (−23.39, −06.99)	2.31 (1.70, 3.30)	0.098 (0.075, 0.125)	0.838 (0.828, 0.866)	3.2, 5.2
prG	−17.37 (−23.30, −0.510)	2.54 (1.40, 5.10)	0.122 (0.090, 0.185)	0.812 (0.786, 0.843)	3.6, 6.1
prG	−16.14 (−22.20, −06.01)	1.40 (0.80, 2.60)	0.082 (0.065, 0.105)	0.848 (0.832, 0.858)	3.1, 4.8
phG	−16.11 (−21.99, −07.18)	2.47 (1.30, 3.50)	0.103 (0.075, 0.145)	0.809 (0.781, 0.830)	3.7, 6.2
phG	−15.81 (−21.43, −0.764)	2.35 (1.50, 3.40)	0.112 (0.085, 0.150)	0.802 (0.783, 0.826)	3.8, 6.5
phG	−15.96 (−22.03, −07.83)	1.83 (0.70, 2.80)	0.081 (0.070, 0.095)	0.841 (0.827, 0.850)	3.2, 5.1
phG	−15.15 (−21.06, −08.05)	2.64 (2.00, 3.60)	0.102 (0.090, 0.110)	0.826 (0.821 0.834)	3.4, 5.6
plmG	−13.54 (−20.54, −02.17)	2.99 (1.60, 6.30)	0.101 (0.070, 0.190)	0.855 (0.848, 0.863)	3.0, 4.7
plmG	−13.71 (−19.88, −04.68)	3.90 (1.90, 5.80)	0.073 (0.060, 0.095)	0.065 (0.849, 0.874)	2.8, 4.3
plmG	−16.78 (−23.38, −03.18)	3.00 (1.50, 6.30)	0.105 (0.075, 0.175)	0.833 (0.820, 0.851)	3.3, 5.3
plmG	−15.25 (−22.50, −05.50)	1.65 (0.80, 3.00)	0.088 (0.060, 0.130)	0.856 (0.834, 0.867)	2.9, 4.6
f	−18.95 (−23.25, −12.85)	2.47 (2.20, 2.80)	0.092 (0.085, 0.095)	0.827 (0.826, 0.827)	3.4, 5.5
f	−20.07 (−24.83, −12.23)	2.00 (1.90, 2.10)	0.122 (0.115, 0.135)	0.803 (0.802, 0.804)	3.8, 6.4
f	−19.74 (−23.82, −10.22)	2.92 (2.80, 3.10)	0.099 (0.095, 0.100)	0.836 (0.834, 0.839)	3.2, 5.2
f	−18.15 (−22.64, −11.83)	2.38 (2.10, 2.80)	0.103 (0.100, 0.105)	0.832 (0.826, 0.836)	3.3, 5.4
vc	−14.43 (−20.90, −05.50)	1.98 (1.00, 3.60)	0.075 (0.060, 0.105)	0.852 (0.846, 0.859)	3.0, 4.7
vc	−15.76 (−20.77, −05.96)	3.07 (1.80, 4.10)	0.091 (0.055, 0.130)	0.848 (0.836, 0.864)	3.1, 4.9
vc	−17.69 (−22.63, −06.63)	2.17 (1.50, 2.90)	0.104 (0.090, 0.120)	0.837 (0.834, 0.842)	3.3, 5.2
vc	−17.25 (−23.57, −03.15)	2.22 (1.60, 2.80)	0.119 (0.105, 0.135)	0.799 (0.795, 0.805)	3.9, 6.6
ef	−14.51 (−21.94, −01.96)	1.78 (1.00, 2.90)	0.155 (0.135, 0.185)	0.761 (0.742, 0.778)	4.7, 8.2
ef	−17.74 (−23.49, −05.88)	1.95 (1.10, 3.10)	0.101 (0.885, 0.130)	0.822 (0.816, 0.829)	3.5, 5.7
ef	−15.61 (−21.53, −06.33)	1.97 (1.30, 2.40)	0.095 (0.080, 0.110)	0.854 (0.846, 0.860)	3.0, 4.7
ef	−14.50 (−20.91, −04.28)	2.46 (1.60, 3.20)	0.083 (0.070, 0.115)	0.860 (0.853, 0.868)	2.9, 4.5
t	−14.49 (−22.44, −02.24)	2.60 (1.70, 3.60)	0.111 (0.075, 0.140)	0.812 (0.808, 0.816)	3.7, 6.1
t	−12.78 (−20.44, −03.64)	1.34 (1.20, 1.60)	0.138 (0.130, 0.150)	0.809 (0.808, 0.809)	3.8, 6.2
pd	−10.88 (−19.26, −01.65)	2.83 (2.30, 3.60)	0.084 (0.079, 0.095)	0.856 (0.854, 0.858)	3.0, 4.6
pd	−12.19 (−19.50, −02.70)	2.52 (2.10, 3.00)	0.082 (0.080, 0.085)	0.833 (0.826, 0.843)	3.3, 5.3
efB	−16.65 (−22.27, −05.07)	3.10 (2.40, 4.90)	0.090 (0.070, 0.115)	0.846 (0.840, 0.854)	3.1 , 4.9
fB_3	−16.38 (−21.87, −09.47)	2.22(1.30, 2.80)	0.084 (0.070, 0.110)	0.834 (0.826, 0.849)	3.2, 5.3
fB_3	−15.83 (−22.25, −08.46)	2.98 (1.70, 4.10)	0.100 (0.080, 0.115)	0.854 (0.843, 0.871)	2.9, 4.6
fB_2	−15.84 (−22.04, −01.82)	2.56 (0.70, 9.70)	0.103 (0.080, 0.145)	0.834 (0.818, 0.864)	3.3, 5.3
fB_2	−15.42 (−21.19, −03.38)	2.10 (1.40, 3.20)	0.084 (0.055, 0.105)	0.856 (0.832, 0.876)	3.0, 4.6
fB_1	−14.82 (−20.22, −06.42)	1.30 (0.70, 2.30)	0.099 (0.080, 0.145)	0.843 (0.838, 0.848)	3.1, 5.0
fB_1	−15.25 (−21.09, −04.69)	2.23 (1.40, 3.30)	0.086 (0.065, 0.095)	0.850 (0.831, 0.869)	3.0, 4.8
fN_2	−17.85 (−23.36, −10.16)	1.92 (1.50, 2.30)	0.147 (0.135, 0.160)	0.809 (0.807, 0.814)	3.9, 6.2
fN_1	−15.17 (−20.56, −08.17)	2.09 (0.30, 5.40)	0.135 (0.075, 0.250)	0.816 (0.776, 0.849)	3.8, 6.0
fI	−08.94 (−14.91, −04.11)	1.50 (1.20, 2.00)	0.110 (0.085, 0.135)	0.838 (0.834, 0.842)	3.4, 5.2
fI	−11.11 (−19.49, −03.48)	2.71 (2.20, 3.10)	0.121 (0.110, 0.125)	0.819 (0.816, 0.821)	3.7, 5.9
pmH	−16.96 (−22.40, −10.20)	3.23 (2.40, 6.30)	0.098 (0.075, 0.170)	0.836 (0.818, 0.858)	3.2, 5.2
vcH_3	−16.62 (−22.71, −05.69)	3.00 (2.10, 3.70)	0.107 (0.095, 0.120)	0.819 (0.815, 0.825)	3.6, 5.8
vcH_2	−16.85 (−23.24, −00.64)	2.06 (1.30, 2.90)	0.101 (0.080, 0.130)	0.835 (0.828, 0.845)	3.3, 5.3
vcH_1	−16.82 (−21.78, −04.18)	3.20 (1.50, 4.70)	0.090 (0.080, 0.100)	0.840 (0.831, 0.849)	3.2, 5.1

THE MAGELLAN MISSION

The Magellan spacecraft orbited Venus from August 10, 1990, until it plunged into the Venusian atmosphere on October 12, 1994. Magellan Mission objectives included (1) improving the knowledge of the geological processes, surface properties, and geologic history of Venus by analysis of surface radar characteristics, topography, and morphology and (2) improving the knowledge of the geophysics of Venus by analysis of Venusian gravity.

The Magellan spacecraft carried a 12.6-cm radar system to map the surface of Venus. The transmitter and receiver systems were used to collect three data sets: (1) synthetic aperture radar (SAR) images of the surface, (2) passive microwave thermal emission observations, and (3) measurements of the backscattered power at small angles of incidence, which were processed to yield altimetric data. Radar imaging and altimetric and radiometric mapping of the Venusian surface were accomplished in mission cycles 1, 2, and 3 from September 1990 until September 1992. Ninety-eight percent of the surface was mapped with radar resolution on the order of 120 m. The SAR observations were projected to a 75-m nominal horizontal resolution, and these full-resolution data compose the image base used in geologic mapping. The primary polarization mode was horizontal-transmit, horizontal-receive (HH), but additional data for selected areas were collected for the vertical polarization sense. Incidence angles varied between about 20° and 45°.

High-resolution Doppler tracking of the spacecraft took place from September 1992 through October 1994 (mission cycles 4, 5, 6). Approximately 950 orbits of high-resolution gravity observations were obtained between September 1992 and May 1993 while Magellan was in an elliptical orbit with a periapsis near 175 km and an apoapsis near 8,000 km. An additional 1,500 orbits were obtained following orbit-circularization in mid-1993. These data exist as a 75° by 75° harmonic field.

MAGELLAN RADAR DATA

Radar backscatter power is determined by (1) the morphology of the surface at a broad range of scales and (2) the intrinsic reflectivity, or dielectric constant, of the material. Topography at scales of several meters and larger can produce quasi-specular echoes, and the strength of the return is greatest when the local surface is perpendicular to the incident beam. This type of scattering is most important at very small angles of incidence, because natural surfaces generally have few large tilted facets at high angles. The exception is in areas of steep slopes, such as ridges or rift zones, where favorably tilted terrain can produce very bright signatures in the radar image. For most other areas, diffuse echoes from roughness at scales comparable to the radar wavelength are responsible for variations in the SAR return. In either case, the echo strength is also modulated by the reflectivity of the surface material. The density of the upper few wavelengths of the surface can have a significant effect. Low-density layers, such as crater ejecta or volcanic ash, can absorb the incident energy and produce a lower observed echo. On Venus, a rapid increase in reflectivity exists at a certain critical elevation above which high-dielectric minerals or coatings are thought to be present. This leads to very bright SAR echoes from virtually all areas above that critical elevation.

The measurements of passive thermal emission from Venus, though of much lower spatial resolution than the SAR data, are more sensitive to changes in the dielectric constant of the surface than to roughness. They can be used to augment studies of the surface and to discriminate between roughness and reflectivity effects. Observations of the near-nadir backscatter power, collected using a separate smaller antenna on the spacecraft, were modeled using the Hagfors expression for echoes from gently undulating surfaces to yield estimates of planetary radius, Fresnel reflectivity, and root-mean-square (rms) slope. The topographic data produced by this technique have horizontal footprint sizes of about 10 km near periapsis and a vertical resolution on the order of 100 m. The Fresnel reflectivity data provide a comparison to the emissivity maps, and the rms slope parameter is an indicator of the surface tilts, which contribute to the quasi-specular scattering component.

SIF MONS QUADRANGLE

The Sif Mons quadrangle of Venus includes lat 0° to 25° N. and long 330° to 0° E.; it covers an area of about 8.10 x 10[6] km[2] (fig. 1). The data used to construct the geologic map were from the National Aeronautics and Space Administration (NASA) Magellan Mission. The area is also covered by Arecibo images, which were also consulted (Campbell and Campbell, 1990; Campbell and others, 1989). Data from the Soviet Venera orbiters do not cover this area.

All of the SAR products were employed for geologic mapping. C1-MIDRs were used for general recognition of units and structures; F-MIDRs and F-MAPs were used for more specific examination of surface characteristics and structures. Where the highest resolution was required or some image processing was necessary to solve a particular mapping problem, the images were examined using the digital data on CD-ROMs. In cycle 1, the SAR incidence angles for images obtained for the Sif Mons quadrangle ranged from 44° to 46°; in cycle 3, they were between 25° and 26°. We use the term "high backscatter" of a material unit to imply a rough surface texture at the wavelength scale used by Magellan SAR. Conversely, "low backscatter" implies a smooth surface. In addition, altimetric, radiometric, and rms slope data were superposed on SAR images. Figure 2 shows altimetry data; figure 3 shows images of ancillary data for the quadrangle; and figure 4 shows backscatter coefficient for selected units. The interpretation of these data was discussed by Ford and others (1989, 1993). For corrected backscatter and numerical ancillary data see tables 1 and 2; these data allow comparison with units at different latitudes on the planet, where the visual appearance may differ because of a different incidence angle. Synthetic stereo images, produced by overlaying SAR images and altimetric data, were of great value in interpreting structures and stratigraphic relations.

MAPPING TECHNIQUES

The techniques of geological mapping of planetary bodies from spacecraft images is well established (for example, Wilhelms, 1972, 1990). The techniques used in constructing the map were modified to accommodate radar images that have their own special characteristics (Ford and others, 1989; Tanaka and others, 1994). Nevertheless, the purpose of our study is to identify rock units, define unit boundaries, interpret unit origins, recognise structures of different types, establish age relations between structures and units, and determine the history of the Sif Mons quadrangle. The general problems of using SAR data were discussed by Ford and others (1993) and will not be repeated here. Specific problems encountered in mapping this quadrangle are, however, discussed.

Units imaged with radar are most easily delineated if they have a distinctly different radar backscatter from the adjacent units. This is not always the case, and some units may not be distinguished on the images if adjacent units have the same or similar backscatter. A young unit superposed on an old unit may not necessarily be recognised if both units have the same surface roughness. Units may be identifiable, however, if they have different dielectric properties. A problem arises when surface characteristics of a material unit change across the outcrop; in some places, the boundary with an adjacent unit is distinguished by different surface properties, but elsewhere the surfaces are similar. What may appear as different units in one area may look like the same unit in other areas. Because lavas, which make up the bulk of this quadrangle, are prone to have different surface textures in different parts of the same flow, this has presented a challenge in unit determination.

The synthetic stereo images (10x exaggeration) were of critical importance in interpreting Venusian topography. For example, many topographic rises representing inliers of older plains materials would not have been easily recognised without using this data set. Embayment relations, as well as ridges associated with the coronae and plains, are well illustrated in the stereo data. The altimetric data were used to interpret the broader scale topography (fig. 2).

GENERAL GEOLOGY

The quadrangle contains the southeast end of Guinevere Planitia, an extensive plains area consisting of a linear depression that, at its deepest part in the map area, is more than 1 km below the mean planetary radius (mpr) of 6,051.84 km (fig. 2; Ford and Pettengill, 1992). Bordering the plains to the northeast is western Eistla Regio, a broad rise at the end of a ridge extending from the western end of Aphrodite Terra and standing about 1.8 km above the floor of Guinevere Planitia (Stofan and others, 1995). Superposed on the rise are the two major volcanic constructs, Sif and Gula Montes, that have areas of 300 km and 400 by 250 km and heights of 2.0 km and 3.2 km above mpr, respectively (Senske and others, 1992).

The geology of western Eistla Regio was first described using Pioneer and Arecibo data (Campbell and Campbell, 1990; Senske, 1990; Senske and others, 1991). Later, using early Magellan data, Senske and others (1992, 1993) identified the following units: ridged terrain; tesserae; bright mottled plains; coronae; volcanic centers; and the large volcanoes, Sif and Gula Montes. The topographic rise and related volcanism is interpreted by many authors as the surface expression of a mantle plume (Senske and others, 1992, 1993; Bindschadler and others, 1992b; Grimm and Phillips, 1992; Stofan and others, 1995). Senske and others (1992) considered three models for the formation of the upland: (1) a simple single plume; (2) multiple upwellings in which Sif and Gula Montes each have separate plumes; and (3) secondary upwelling from a single plume, giving rise to different volcanic centers.

The relation between gravity and topography provides an indication of the mechanism that supported the surface features of the region (Stofan and others, 1995). Gravity data from the Pioneer Venus Mission reveal a positive free-air anomaly situated over the rise, centered on Gula Mons, corresponding to between 45 mGal and 60 mGal (Grimm and Phillips, 1992; Bindschadler and others, 1992b). This equates to an apparent depth of compensation on the order of 200 km. These observations are consistent with a mantle plume situated beneath western Eistla Regio (Grimm and Phillips, 1992; Bindschadler and others, 1992b; Smrekar, 1994; Stofan and others, 1995).

Also considered a manifestation of plume activity is Heng-o Corona (Barsukov and others, 1986; Stofan and others, 1991). Heng-o Corona was first identified in Venera 15 and 16 data (Barsukov and others, 1984). Corona is a morphologic term applied to circular and elongate structures observed on Venus and defined by an annulus of concentric fractures and ridges associated with varying amounts of volcanism (Barsukov and others, 1986; Pronin and Stofan, 1990; Stofan and others, 1992, 1995, 1997; Copp and others, 1998). Heng-o Corona dominates the southeastern part of the quadrangle and is the second largest corona on Venus with a mean diameter of 965 km. Heng-o Chasma is an arcuate trench that forms the northern part of Heng-o Corona. The chasma deforms the surrounding Guinevere plains and, hence, postdates plains formation. Heng-o Corona is, thus, relatively young, contrary to previous interpretations (Sandwell and Schubert, 1992). The history of Heng-o Corona is protracted (Copp and others, 1998); a number of phases of volcanic and tectonic activity are recorded within the interior of this corona. Six other major coronae are observed within the quadrangle.

STRATIGRAPHY

Tesserae Material

The material has a high radar backscatter, consisting of blocks approximately 35 km across demarcated by linear troughs. All of the outcrops consist of inliers rising above the surrounding plains and are embayed by plains units. The surfaces used to identify this material unit were originally termed "tessera" based on the Soviet Venera SAR data (Barsukov and others, 1984, 1986). The term "complex ridged terrain" has been used by some authors (Solomon and others, 1992; Bindschadler and others, 1992a), but even this term does not fully describe the morphology of this material unit. We use the term "tessera material" (unit t). There are only two small exposures of unit t in the quadrangle. Because this unit is characterized by its structural deformation (Hansen and Willis, 1996), there is no certainty that the unit has the same age throughout Venus or within this quadrangle. Tesserae may predate all the plains units as suggested by some (Bindschadler and Head, 1991; Basilevsky and Head, 1995a,b), but in the Sif Mons area, the small patches that occur are embayed only by Guinevere regional plains material. Thus, it can only be determined that tessera material in this quadrangle are pre-Guinevere regional plains in age.

Plains Material

We identify four distinct types of plains units within the quadrangle: deformed plains material (unit pd), Guinevere lineated and mottled plains material (unit plmG), Guinevere homogenous plains material (unit phG), and Guinevere regional plains material (unit prG).

Deformed plains material (unit pd) has a high radar backscatter and, as the name implies, is typically deformed by both extensional and compressional structures. Material that cannot confidently be identified as tesserae is named deformed plains material. Within the map area, deformed plains material is embayed by plains material. Deformed plains material may well have undergone similar deformational processes as tessera material, but the small outcrop size makes the relation between styles of deformation within the unit difficult to establish.

Guinevere lineated and mottled plains material (unit plmG) makes up about 25 percent of the surface area of the quadrangle; most of the unit is found in one large exposure in the northwestern area of the quadrangle. Numerous small volcanic edifices, most of which are shields less than 10 km across, give the unit a mottled appearance and play an important role in characterizing the unit, which often has a different backscatter from the adjacent materials. The density of edifices within the unit is variable. In some areas, the edifices are clustered into distinct groups and are mapped as edifice fields (unit ef). Other areas show only isolated edifices.

Material that constitutes unit plmG is generally highly deformed by closeley spaced parallel faults, and some of its outcrops are ridges rising above the surrounding plains. The unit also contains numerous narrower wrinkle ridges and lineaments. Wrinkle ridges are particularly evident at lat 17.5° N., long 336° E. Close inspection of full-resolution data reveal a fine-scale polygonal fracturing with fractures that have a separation of just a few kilometers. Polygonal fracturing is particularly evident in the northwestern area of the quadrangle, for example at lat 22° N., long 334° E., northwest of Aurelia crater (20.3° N., 331.8° E.). Superposed on the small-scale polygonal fracturing are wrinkle ridges and longer, more linear northwest-southeast-trending fractures, considered by some to be the surface manifestation of dikes (McKenzie and others, 1992).

Unit plmG crops out at a greater elevation than the surrounding plains units. Unit plmG is identified as the oldest plains material because it is embayed by plains units phG and prG. Embayment of unit plmG by unit prG is seen along the contact of the two units near lat 19° N., long 335° E. Fractures that deform unit plmG are truncated by the younger plains material. The embayment at this and other contact locations is more clearly resolved by the stereo data. The age relation between unit plmG and the numerous volcanic centers and edifice fields (ef) is more difficult to ascertain. Most appear to have formed either contemporaneously with or after unit plmG.

The Guinevere homogenous plains material (unit phG), which covers about 10 percent of the quadrangle, is named for the uniform backscatter over large areas. Exposures of unit phG are mainly confined to the southwestern area of the quadrangle and form volcanic plains, which are essentially featureless apart from flow features that are most evident at the margin of the unit. The morphology of the margins is the primary evidence for these materials being composed of volcanic flows. Stereo data shows that the largest exposures of units phG and plmG have been tectonically warped. However, in contrast to unit plmG, unit phG has undergone less faulting and fracturing. Where unit phG and unit plmG are in contact, it is common for unit phG to embay unit plmG.

The Guinevere regional plains material (unit prG) has a low backscatter, giving a darker appearance at the incidence angle of these images than the other plains units. The unit is extensive, making up 40 percent of the surface of the quadrangle. Unit prG appears almost featureless except for superposed wrinkle ridges. The unit's homogeneity is considered to reflect its formation from lava flows of considerable spatial extent. However, in local areas, ill-defined circular features are observed and sometimes have central pit-like expressions. These features may indicate the presence of low-angle shields composed of lavas with smooth surfaces. We consider that such "stealth shield volcanoes" are poorly delineated because their radar characteristics are very similar to the plains in which they occur (Copp and Guest, 1995; Copp, 1997). If this is the case, then at least parts of unit prG may be composed of coalescing shields whose boundaries are not visible in the SAR images, because all flow surfaces have the same radar backscatter as the plains material. The spatial extent of such shields is difficult to estimate. Unit prG embays unit phG indicating that it is younger.

The phG material is interpreted to consist of extensive lava sheets whose sources are not detectable in the SAR images. By contrast, the prG material has not only extensive lava sheets but also clusters of small shields, some of which may mark the source of the more extensive lava sheets. Unit plmG material is dominated by small shields.

Isolated Flow Material

Isolated flow material (unit f) consists of patches of volcanic material that occur in the southern part of the quadrangle. Individual exposures range in size from about 10 km to 180 km, with a typical size of about 40 km across. Unit f has a range of backscatters lower than that of underlying units prG and phG. Unit f flow material is interpreted on the basis of the low backscatter to have a smooth surface texture. The very smooth surface suggests rapid emplacement before a sustained crust could develop (Guest and others, 1995). At least one of these flows was fed from a canale. Some of the flows have been modified by surficial materials from the impact crater Kodu (lat 0.9° N., long 338.7° E.) and possibly Clio (lat 6.3° N., long 333.5° E.), which alter their radar backscatter to higher values. Other flows in the same area have not been altered and are much darker. This implies that some of the isolated flows predate these craters, whereas others postdate them.

Edifice Flow Material and Steep-sided Domes

Isolated shield-like volcanoes are scattered throughout the quadrangle, and a representative selection of these is indicated on the map. Because the shields have low-angle flanks of just a few degrees, they are difficult to see in the SAR images, unless there is a considerable surface textural difference between the shield and the surrounding plains. However, the summit pits are typically much more pronounced, with a high backscatter; clusters of pits on the plains usually indicate the presence of shields only faintly indicated by radar backscatter. Some of the plains units may be constructed from coalescing shields similar to some on Earth, such as the Snake River Plain in Idaho (Greeley and King, 1977). Some edifices can be related to fracture belts.

Edifice fields are characterized by clusters of volcanic constructs that are generally less than 10 km in basal diameter as described by Guest and others (1992). The majority of the constructs have flank slopes less than 5° and, by terrestrial standards, would be shield volcanoes; some are steeper and have a cone-like or dome-like morphology. They show a range in radar backscatter values.

Collections of edifices are mapped as edifice field material (unit ef). Fourteen edifice fields are mapped in the Sif Mons quadrangle. They are mapped on the assumption that edifices contained within the field share a common source. The contact boundaries of these units are defined by either flow material associated with the edifices or by edifice density. Where boundaries are difficult to confidently delineate, a dashed line has been used. Edifice fields differ from the mapped volcanic center material (unit vc), which typically consists of one large central volcano. Within the quadrangle, the stratigraphic position of individual edifice fields is variable, forming throughout the emplacement of the major plains units.

Edifice fields tend to have diameters of about 100 km. A typical number of shields for a single field is about 75. In some cases, the fields are surrounded by an apron of flows that may extend as far as 275 km from the center of the field. Structurally, edifices may or may not be associated with fracturing. If fractures are observed, the pits of many edifices are often elongated in a similar orientation to the fracturing. Where fractures are present within an edifice field, edifices typically both postdate and predate the deformation.

Only two steep-sided domes occur in the map area and both are less than 20 km across. Both postdate fractures associated with the formation of Heng-o Corona. Originally, steep-sided domes were interpreted as having been produced by the eruption of lava with a high effective viscosity comparable to rhyolite on Earth (Head and others, 1991; Guest and others, 1992; Pavri and others, 1992). However, Anderson and others (1994) and Plaut and others (1994) show that there are significant morphological, volcanological, and remote-sensing differences when compared to terrestrial silicic domes. Venusian domes are at least an order of magnitude larger than terrestrial domes and have much smoother surfaces, indicated by considerably lower rms slope values. From these observations we conclude that either Venusian domes do not consist of silicic lavas or silicic volcanism does not operate in the same way on Venus and Earth (Plaut and others, 1994).

Volcanic Center Material

Volcanic center material (unit vc) relates to volcanic centers generally less than 100 km across with a conical construct normally topped by a crater (<1 km in diameter) or caldera (>1 km in diameter) with flanks constructed of volcanic flow materials that are largely controlled by the local topography. The flows have intermediate to low backscatter, and each center is essentially uniform. Some have associated small edifices and pits within the apron area. As with edifice fields, volcanic centers appear randomly distributed across the quadrangle.

The majority of the volcanic centers superpose the formation of plains materials. However, as with other units on Venus, the relative age of volcanic centers is difficult to assess because their boundaries do not coincide. For each volcanic center, only a local relative age may be established with confidence. The observed stratigraphic range of this unit coincides with the formation of unit plmG and postdates unit prG.

Large Volcanic Shields

Sif Mons material (unit eS) and Gula Mons material (unit eG) are associated with the two large shield volcanoes Sif and Gula Montes, which lie in the northeastern part of the quadrangle; the northern, lower parts of their flanks lie in the adjacent quadrangle (V–19), whereas the eastern, lower flank of Gula Mons falls in the quadrangle to the east (V–20). Both have flanks with slopes less than 1.4° (Senske and others, 1992).

Sif Mons has a nearly circular caldera about 45 km across. It is almost completely filled with younger lavas, and only the south rim is visible. The east rim is the lowest, and a fan of lava has breached the caldera rim on this side. Lavas filling the caldera erupted from a vent marked by pits on the northwest edge of the structure. This center has built up above the caldera rim, and lavas have flowed down the upper flanks of the volcano as well as into the caldera. The intra-caldera flows have an intermediate backscatter, but some of the older flows from the caldera on the west and north flanks have a very low backscatter. Radial rows of aligned pits extend down the upper part of the volcano on the southeast side.

The caldera of Sif Mons surmounts a summit cone of the volcano. This cone, which has steeper sides than the volcano's outer flanks, has a basal diameter of about 170 km. It appears to have been built by flows from the summit; these flows extend to the foot of the summit cone or just beyond. A general progression of younger upper flank flows lie on older lower flank flows (Copp, 1997; Stofan and others, 2001).

Many flows erupted from flank vents. Some are long, thin flows, whereas others form a fan of lavas that built a thick pile in the flank vent area, forming a well-defined, shield-like hill with a summit pit. The flank flows show a range of backscatter from low to high. Apart from scale, the general form of Sif Mons is similar to basaltic volcanoes such as Mount Etna in Sicily. Mount Etna is about 40 km across and owes its conical profile to regular eruptions generating short flows from the summit and less frequent eruptions often producing longer flows from flank vents. Thus, the summit grows faster than the flanks (Guest and Murray, 1979). It is likely that Sif Mons grew under similar conditions, with a continuously open central conduit and occasional flank eruptions (Copp, 1997; Stofan and others, 2001).

Because the diameter of a caldera is roughly comparable to or less than the diameter of the underlying magma reservoir (Ryan and others, 1983), we interpret the magma reservoir of Sif Mons to be at least 40–50 km across. This is to be expected, as many flows are over 250 km long and, therefore, have a large volume. Low-radar-backscatter deposits that locally surround the small flank craters may represent pyroclastic activity (lat 21.4° N., long 352.7° E.). The deposits have their greatest extent downslope but always totally surround the flank craters. The boundaries of these deposits are diffuse (Copp, 1997; Stofan and others, 2001).

Gula Mons is, in many ways, different from Sif Mons. Its summit has a northeast-trending, 100-km-long rift zone with a width of about 30 km. At either end is a volcanic center, each consisting of a lava-filled, roughly circular caldera. The caldera at the southwest end is about 35 km across, whereas the northeast one is about 25 km across. From the northeast caldera, a graben-like rift cuts down the north flank of the volcano into Idem-Kuva Corona.

A high percentage of the Gula Mons lava flows, some of which are at least 400 km long, erupted from the rifts or the calderas. Thus, it appears that Gula Mons had a different plumbing system from that of Sif Mons, with much of the eruptive activity restricted to the summit area and with a different overall flow morphology (Copp, 1997; Stofan and others, 2001).

The age relations between Sif and Gula Montes are hard to determine. At least one Gula Mons flow appears to be superposed on a flow from Sif Mons. However, this only gives the relationship between those two flows and not between the two constructs. It is possible that these two major volcanic centers were penecontemporaneous. A terrestrial analogue, but on a much smaller scale, could be Nyragongo and Nayalmagira in Zaire (Simkin and Siebert, 1994), which are both active, often simultaneously. But relative ages of Sif and Gula Montes could not be determined from photogeology.

Coronae

Coronae are structures that normally consist of a circular to subcircular ridge often surrounded by an outer moat and, in some cases, an inner one. An annulus of deformation is nearly always associated with the ridge and moat (Pronin and Stofan, 1990; Stofan and others, 1991, 1992; Janes and others, 1992; Squyres and others, 1992). Flows often extending from fractures are associated with these structures (Roberts and Head, 1993). Coronae have been interpreted as the surface expression of thermal plumes (Barsukov and others, 1986; Stofan and others, 1991, 1992; Squyres and others, 1992). There are seven coronae in the Sif Mons quadrangle, listed in descending order of size (Copp and Guest, 1995; Copp and others, 1997, 1998): Heng-o (lat 2.0° N., long 355.5° E.), Benten (lat 14.2° N., long 341° E.), Silvia (lat 12.5° N., long 355.5° E.), Nissaba (lat 26° N., long 355° E.; just north of map area), Idem-Kuva (lat 25° N., long 358° E.), Eingana (lat 5.0° N., lat 350.0° E.), and Chiun (lat 18.3° N., long 340.5° E.). Corona structures and associated volcanism represent mappable units that have protracted histories.

Heng-o Corona is the largest in the quadrangle with a maximum diameter of 1,200 km. The south margin lies outside the quadrangle in V–43 (Greeley and others, 1994; Bender and others, 2000). Heng-o Corona formed from a protracted and complex sequence of events (Copp and others, 1997, 1998). It is roughly circular in plan view. Initial deformation of unit prG is now preserved as closely spaced grabens within the annulus of Heng-o Corona. Pronounced ridges and troughs then formed concentrically around the structure but not always coinciding with the earlier fracture trend. The north margin of Heng-o Corona consists of two prominent troughs (Heng-o Chasma) separated by a prominent ridge reaching 1 km in height. The crest of the ridge shows little deformation. The occurrence of an outer and inner trough separated by a narrow ridge is also seen to the southeast and southwest of Heng-o Corona. To the west, it is bordered by a narrow, lower ridge. Eingana Corona, a smaller corona-like feature with associated volcanism, exists to the northwest of Heng-o Corona.

Deformation of the annulus was followed by the development of a complex volcanic center (unit vc) filling the smaller corona Eingana. Flow material from this volcanic center is controlled and, in places, superimposes the annulus deformation of Heng-o Corona. The oldest manifestation of volcanism seen within the annulus of Heng-o Corona is represented by a central-vent volcano with a summit caldera ringed by small edifices (Heng-o volcanic center material 1, vcH_1). The age relation between unit vcH_1 and the Eingana volcanic center is not apparent. Nor is the stratigraphic relation between unit vcH_1 and an area of mottled plains, mapped as Heng-o mottled plains material (unit pmH). Stereo data do show that unit pmH is deformed by later structures associated with the formation of Heng-o. A second volcanic center, Heng-o volcanic center material 2 (unit vcH_2), is seen to superpose unit vcH_1. Next, the interior of Heng-o Corona was deformed by northwest-trending fractures. These fractures deform units vcH_1, vcH_2, and pmH but are superposed by Heng-o volcanic center material 3 (unit vcH_3), another volcanic center located on the western floor of the corona.

It is apparent that Heng-o Corona and the smaller corona-like feature (Eingana Corona) deform the youngest (unit prG) of the widespread plains units in the area and exhibit post-deformational effusive volcanic activity; this implies a younger age than the previously suggested age of Heng-o as an older type corona situated within low-lying plains (Sandwell and Schubert, 1992).

As with Heng-o Corona, Benten Corona has a complex structure and history (Copp and others, 1998). The main structure is kidney shaped in plan view and has a maximum diameter of 250 km. It consists of a ridge that is cut by closely spaced concentric fractures. The interior hollow has an irregular floor that is cut by north-south fractures. The southern part of the rim is breached by a southeast-trending graben that has a width of 50 km. Just outside the main structure on the southwest side are two smaller corona-like features. The north feature is almost a complete ring, whereas the south one is incomplete and appears to be truncated by the other.

Surrounding most of Benten Corona is an apron of lavas, composing Benton flow material 1 (unit fB_1), which extends as much as 460 km from the outer edge of the structure to the west and south and lies on unit prG. A second set of lavas, Benten flow material 2 (unit fB_2), erupted from the north margin of the corona structure, postdating unit fB_1. Unit fB_2 material flowed both into, indicated by the truncation and flooding of interior north-trending grabens, and out of the corona structure, was subsequently deformed by the uplift of the corona ridge, and, at least in part, predated ridge deformation. A third set of flows, Benton flow material 3 (unit fB_3), extends from the concentric fractures on the crest of the ridge that forms the west and east sides of the structure. This younger material has a more digitate morphology and is less extensive than the earlier aprons, fB_1 and fB_2. An edifice field (unit efB) is located within the southern area of the central depression of Benten Corona; flows from this field are controlled by the large southeast-trending graben and postdate unit fB_3.

Silvia Corona is approximately 300 km across; its flows are mapped as Silvia Corona material (unit S). It both predates the surrounding unit prG and is embayed by it. It forms a topographic high with respect to the surrounding plains and is bordered by an arcuate ridge on the north side. There are contiguous hills in the center, and there is a circular hill about 50 km across on the south side. Silvia Corona was clearly formed by a long-lived event, because the annular structural ridges also deform the surrounding unit prG; deformation continued after the last of the volcanism from Silvia Corona (Copp and others, 1998).

Nissaba Corona, which lies just north of the map area, has an irregular topography seen in plan view (the northwest-southeast axis measures approximately 320 km, with a north-south axis of 220 km), with a central circular plateau and smaller topographic high to the northwest. To the west and southwest, the central rise is surrounded by a trough, which shallows to the east. Outside the trough, to the southwest, is a broad ridge that curves into the central region of Nissaba. The ridge is discontinuous around the corona and no outer trough is observed.

A central volcano, at lat 26.0° N., long 354.5° E., just north of the quadrangle, is the source of a radial, ill-defined unit mapped as Nissiba flow material 1 (unit fN_1), which covers a significant portion of Nissaba's northwest section. The volcano and surrounding flow material is associated with the formation of Nissaba Corona (Copp and others, 1997, 1998). Postdating unit fN_1 is an extensive apron of flows, Nissaba flow material 2 (unit fN_2), seen on the west, southwest, and south topographic rim of the corona. The flows emanate from fractures that surround a circular depression within Nissaba. Nissaba Corona is embayed by regional plains material that has a radar appearance and stratigraphic age equivalent to prG and that constitutes Sedna Planitia to the north (V–19) of this quadrangle, described by Copp (1997) and Copp and others (1998).

The south and southwest ridge of Nissaba Corona acts as a topographic barrier to Sif and Gula flow materials, which existed before emplacement of these flows. To the southwest, flows that erupted from fractures associated with Nissaba (unit fN_2) are overlain by Sif Mons material units. However, at the south margin of the corona, Nissaba flow material has a more ambiguous relation with surrounding units. Some Nissaba flow lobes may postdate adjacent early Sif or Gula Montes material units, suggesting that Nissaba late-stage volcanism may postdate emplacement of some Sif and Gula material units.

Idem-Kuva Corona lies on the northeast edge of the quadrangle directly north of Gula Mons. It has a diameter of about 250 km; only half of it lies in this quadrangle. It consists of a semicircular ridge that deforms flows of the north flank of Gula Mons. Inside the ridge is a moat surrounding a central hill of older material mapped as Idem-Kuva relic plains material (unit prI) that is about 100 km across and rises to 600 m above the surrounding topography, approximately the same height as the highest part of the ridge structure. Both the ridge and the moat are cut by closely spaced concentric fractures. Some arcuate grabens, associated with the southwest annulus of Idem-Kuva, do not coincide with the larger scale topographic rim but are clearly offset outboard, which is evidence for a protracted structural development of this corona (Copp and others, 1997, 1998). The south side of the corona is cut by a deep graben-like rift that is incised into the north flank of Gula Mons and extends to the northeast summit caldera. The observation that the southern structures of Idem-Kuva Corona cut the flanks of Gula Mons shows that this section of the corona is younger and is one of the youngest major structures in the quadrangle. Previous work (Senske and others, 1992, 1993) suggested Idem-Kuva was older than Gula Mons.

Two digitate flows extend into the map area from Idem-Kuva and are mapped as Idem-Kuva flow material (unit fI). Both have a high radar backscatter. The west flow appears to originate from a small edifice situated at approximately lat 24.3° N., long 358° E., whereas the east flow originates from grabens located at approximately lat 24.5° N., long 358.5° E. These flows are controlled by the topographic structure of Idem-Kuva Corona and superpose the materials of Sedna Planitia to the north (V–19). They represent late-stage volcanic activity associated with Idem-Kuva.

Some geologists suggest a specific age of formation for coronae on Venus using both local stratigraphic relations (Basilevsky and Head, 1995a,b; Basilevsky and others, 1997) and crater density statistics (Price and Suppe, 1994; Namiki and Solomon, 1994; Price and others, 1996). Basilevsky and Head (1995a,b) and Basilevsky and others (1997) argue that specific stages of corona evolution are represented by units normally contemporaneous on a global scale. However, coronae seen within the V–31 map area (and extending north into V–19) do not show simple relations between structural deformation and time (Copp and others, 1998). Using cross-cutting structural relations and extrusive flow material superposition gathered from high-resolution and stereo imagery, a stratigraphy of the coronae in V–31 is presented in the Correlation of Map Units. Idem-Kuva and Heng-o Coronae show evidence of more than one phase of annulus formation. Some corona annuli are younger than the regional plains (Heng-o), whereas others are older (Nissaba). Similarly, interior deformation is not always relatively old at the coronae studied here (Benten). The different stages of corona evolution were not simultaneous in this map area, nor were the same processes repeated at another corona (Copp and others, 1998).

We establish that three (Nissaba, Idem-Kuva, and Silvia) of the five coronae began forming before or during the materials of the regional plains were deposited in the map area (Copp and others, 1998). Deformation and volcanism associated with Idem-Kuva Corona continued after the formation of Gula Mons material units. Whereas some coronae may predate large shield volcanoes (McGill, 1994), our studies indicate that simple relations between the relative ages of coronae and large volcanoes (Price and others, 1996; Namiki and Solomon, 1994) should be used with caution.

Crater Material

There are 19 mappable impact craters in the quadrangle, and we define 4 mappable crater units: crater ejecta material (unit ce), crater floor material (unit cf), crater peak material (unit cp), and crater margin material (unit cm). The size of craters observed ranges from 53 km across at Cunitz crater (lat 14.5° N., long 350.9° E.), with ejecta extending a maximum of 30 km from its crater rim, to approximately 7 km across at Oksana crater (lat 11.9° N., long 352° E.). Rock units associated with Venusian impact craters have characteristics that are unique to this planet (Phillips and others, 1992; Schaber and others, 1992; Schultz, 1992). Like impact craters on other planets, above a critical diameter of about 15 km on Venus (Phillips and others, 1992), craters show central peaks and have terraced inner walls. The high radar backscatter observed would suggest that these structures have rough surfaces. The floors of craters above 30 km contain low-radar-backscatter material, which is considered to represent impact melt.

The surface morphology of ejecta on Venus differs from that associated with craters on any other known planetary body. There are three main facies (Phillips and others, 1991, 1992; Schaber and others, 1992; Schultz, 1992). The rim has a high radar backscatter and appears to be hummocky at the kilometer scale; this is interpreted as being formed during the last stage of crater excavation by overturning, similar to crater rims on the Earth and the Moon (Gault and others, 1968). Outside the rim is a high-radar-backscatter ejecta sheet with a feathery, lobate outer margin. This differs in morphology from the continuous ejecta sheets around craters on all other planets (Phillips and others, 1991). It is interpreted as having formed by turbulent flow of ejecta resulting from interaction between the falling curtain of ejecta on ballistic trajectories and the dense atmosphere as demonstrated in laboratory experiments (Schultz, 1992). This ejecta sheet is normally asymmetric, with a distinct sector where no ejecta was emplaced. This asymmetry is considered to be the result of atmospheric effects, induced by the bolide driving through the atmosphere at an angle to the surface, that modify ejecta trajectories (Schultz, 1992).

Many craters have flow-like deposits that extend outward from the continuous ejecta and follow the topography. An example from Sif Mons quadrangle is Enid crater (lat 16.6° N., long 352.2° E.). Flow material from Enid is controlled by fine-scale fracturing. Crater flow material has been interpreted as impact melt that flowed away from the crater (Schultz, 1992), generally on the downrange side of the crater impact, and formed contemporaneously with the impact.

Surrounding many of the craters is a radar high- or low-backscatter halo. In some cases the distribution of the low-backscatter haloes is controlled by surface features such as wrinkle ridges (for example, Cunitz, lat 14.5° N., long 350.9° E.). Cunitz is also an example of a crater surrounded by a high-radar-backscatter halo. Except where bounded by topographic obstacles, these haloes have indistinct boundaries suggesting that they thin with distance from the crater. The low-backscatter haloes are interpreted as thin deposits of fine-grained debris (Shultz, 1992; Campbell and others, 1992). The high-backscatter haloes may represent surface disturbance creating a rougher surface (Shultz, 1992; Campbell and others, 1992). The crater Aurelia (lat 20.3° N., long 331.8° E.) has a classic low-radar-backscatter parabola around it that opens to the northwest. Such features probably form as a result of the interaction between atmospheric motions and dust particles lofted into the atmosphere (Shultz, 1992). There is no evidence, as suggested by Arvidson and others (1991), that the presence of a parabola indicates the youth of a crater. In this quadrangle, there is no evidence that other craters once had parabolas.

In the south-central part of the quadrangle, dark linear streaks (lat 2.0° N., long 340.5° E.) that fan northeast from Comnena crater (lat 1.2° N., long 343.7° E.) are interpreted as low-radar-backscatter impact debris redistributed by aeolian activity (Greeley and others, 1992). Full resolution images show the radiating streaks in detail.

STRUCTURES

Faults, Grabens, and Rifts

Apart from materials associated with impact craters, all units within the quadrangle have been subjected to some degree of deformation. Least deformed is the isolated flow material (unit f), owing mainly to its small surface area. Both normal faults and graben structures cut many units. Grabens are typically 1 km or less across and normally occur in groups. They have a high-radar backscatter, possibly because of rough talus slopes.

Guor Linea is a major Venusian structure that is best developed in the adjacent Sappho quadrangle (V–32) to the east (Senske and others, 1992; McGill, 1994). Its northwest end extends into the Sif Mons quadrangle. It is superposed by the outermost flows of Gula Mons, which is probably related to this rift structure. In the quadrangle, this rift is a raised structure consisting of uptilted smooth plains on the flanks of Gula Mons with a 70-km wide crest cut by numerous faults. The graben, which is on the southern side of the rift, splays towards the northwest. The rift between Gula Mons and Idem-Kuva Corona follows the same trend but is younger than Gula Mons.

Continuous curvilinear lineaments that are less than 1 km across and extend for hundreds of kilometers are interpreted as grabens developed over dikes, which failed to reach the surface over most of their length (McKenzie and others, 1992). A swarm of dikes is observed in the northwestern portion of the quadrangle, and they are also seen on Gula Mons and occasionally on the plains. Observations elsewhere on Venus provide examples of lavas that have erupted from such features (Lancaster and others, 1995).

Ridges

Intense deformation produced pronounced ridges typically 5 km across and a few hundreds of meters high. Unit plmG has been deformed to produce such ridges, the most striking of which forms a broad arc roughly concentric to Benten Corona. This large structure deforms unit plmG, which was then superposed by unit prG. However, deformation must have continued after emplacement of unit prG, because it too has been deformed to a lesser extent by the same structure. Ridges are associated with all the coronae and deform units of different ages.

Wrinkle Ridges

A pattern of interconnected wrinkle ridges covers most of the quadrangle and is a distinguishing characteristic of the plains units, in particular unit prG. The ridges are between tens to hundreds of kilometers long and have widths of less than about 2 km. They tend to have a high radar backscatter. Their morphology resembles wrinkle ridges on the Moon, Mars, and Mercury (McGill, 1993). Although ridges trend in many directions, there is a dominant trend in a northwest direction across the quadrangle. The origin of wrinkle ridges on other planetary bodies is complex, but they are generally considered to be the result of compressional forces (McGill, 1994).

GEOLOGIC HISTORY

The history of this region is dominated by volcanism and tectonism, accompanied by impact cratering and the relatively minor effects of wind. A wide variety of landforms have been produced. There is no evidence that any one style of volcanic or tectonic activity prevailed at a specific time as suggested by Basilevsky and Head (1995a,b) and Basilevsky and others (1997) but refuted by Copp (1997) and Guest and Stofan (2000), who argue for a more nondirectional history. Volcanism occurs mainly as small edifices, volcanic centers, extensive lava sheets, and corona-generated eruptive products. These differing styles of volcanism appear to have occurred during much of the time represented by the exposed rocks in the quadrangle. Tectonic activity also appears to have been essentially continuous during the history of the area. Typical of volcanic terrains, although extensive units can be dated relative to one another by superposition relations, small isolated volcanoes and other volcanic deposits can only be identified as younger than material on which they lie.

Tessera material, which has suffered multiple phases of deformation, is generally considered to be the oldest material on Venus. In the Sif Mons quadrangle, only three outcrops of this material are observed; two outcrops are embayed only by the Guinevere regional plains material (unit prG) and one outcrop is deformed by both Guinevere plains material (unit prG) and plains material (unit pd). In this area, therefore, we can only confirm that tesserae are older than unit prG material. They, therefore, represent multiple deformed material that is older than any other unit represented in the quadrangle or locally deformed material associated with, for example, a corona within the exposed sequence of rocks older than prG material. If the former is the case, then tessera material in the quadrangle are basement rocks that have been strongly deformed.

Another type of tectonized material unit, the deformed plains material (pd), also forms as small inliers within unit prG and appears to be embayed by plmG. At one inlier it embays tessera material but is embayed by plmG, implying that tessera material is the oldest exposed rock at that site.

Most of the exposed geology of the quadrangle consists of plains materials interpreted to have a volcanic origin. The oldest plains material after the deformed plains (pd) is the lineated and mottled plains material (plmG). This unit contains numerous small volcanic edifices, mainly with a shield-like form, that have diameters as much as about 5 km. It is not clear if lava erupted from other sources to form flows in areas where shields are less abundant. Also, because shield formation continued throughout the subsequent history of the area, some of the shields could postdate unit plmG. This unit has been uplifted as part of the Eistla Regio rise. The plmG material is cut by several types of structure that postdate it but are older than prG materials. These include ridges, grabens, and fractures, together with a few wrinkle ridges.

The subsequent plains units occupy the lowland region (Guinevere Planitia) south of Eistla Regio. Sheets of lava, presumably erupted from fissures, form the homogeneous plains material (phG), overlain by the youngest and most extensive unit, the regional plains material (prG). Unit prG is a time-marker horizon, because it is the most extensive unit in the map area and embays or is embayed by most units. It is interpreted to have been formed by extensive lava flows and small volcanic shields and deformed by wrinkle ridges that are more abundant than on underlying units. This implies that the wrinkle ridge process is specific to prG materials, unless the SAR images are suppressing these features on other unit surfaces with higher backscatter. Silvia Corona predates emplacement of prG material that embays it; but late stage deformation associated with Silvia Corona later warped prG materials where they embay it. Idem-Kuva Corona also started to form before the emplacement of the prG materials, as indicated by its superposition over corona materials north of the map area, but it continued to produce lavas that overlie prG material.

Following emplacement of prG materials, small, isolated flows erupted in the planitia; one is visible at the terminus of a canale. Edifice field material (unit ef) also continued to form, in some cases erupting lava that flowed for hundreds of kilometers. Also intermediate central volcanoes (<100 km in diameter) formed on older deposits; but their age is not constrained and they may be older than prG material.

Following emplacement of the Guinevere regional plains material (prG), two major types of features were formed: a corona and major volcanoes more than 150 km across. The Heng-o Corona structure deformed Guinevere regional plains material, forming an encircling raised rim within which three central volcanoes erupted and fracture belts formed contemporaneously. Lava flows also erupted from the ring structure outside the corona.

Benten Corona also had a complicated history. It lies within a semi-circular ridge of deformed prG material that may represent its earliest stage of formation. The deformed rim of this caldera was either preceded by extensive lava production or accompanied by it. Less extensive volcanism followed.

Age relations between the two major volcanoes, Sif and Gula Montes, are not clear. Lavas on the periphery of both constructs overlie prG material, but it is possible that older lavas within the pile predated prG emplacement. In one place, lavas from Gula Mons appear to overlie a lava from Sif Mons, indicating the age relation between these two flows but not necessarily between the two volcanoes. It is possible both volcanoes grew penecontemporaneously. The age relations between Idem-Kuva Corona and Gula Mons are also intertwined: both growing and rifting partly at the same time. Gula Mons formed over the Guor rift with which it is associated. Guor Linea too deforms prG materials and extends into the adjacent Sapho quadrangle (V–32).

The impact cratering history is not easy to determine. Only one crater is embayed by a lava flow. However, there is evidence for interbedding of impact debris with a sequence of post-prG lavas.

Within the Sif Mons quadrangle, there is little evidence for the style of volcanism and tectonism through time. Formation of large-volume lavas and small edifices occurred throughout the post-tessera history of the map area. Deformation by folding and fracturing has been a universal process. The large shields of Sif and Gula Montes are unique to the area and probably owe their presence in both space and time to the uplifting process of Eistla Regio (Senske and others, 1992). Coronae are the result of protracted activity and formed at different times from at least pre-unit prG to some of the youngest activity.

ACKNOWLEDGEMENTS

We thank the mappers of the surrounding quadrangles (Ronald Greeley, Kelly Bender, David Senske, Ellen Stofan, David Crown, George McGill) and Antony Brian and Simon Tapper for valuable and scientifically stimulating discussions. The work was funded by a postgraduate fellowship awarded to Duncan L. Copp from University College London and by grant GR/01879 awarded to John E. Guest from the United Kingdom Natural Environment Research Council (NERC).

REFERENCES CITED

Anderson, S.W., Crown, D.A., Plaut, J.J., and Stofan, E.R., 1994, Surface characteristics of steep-sided domes on Venus and terrestrial silicic domes—A comparison [abs.], *in* Lunar and Planetary Science Conference, 25th, March 1994: Houston, Tex., Lunar and Planetary Institute, p. 33–34.
Arvidson, R.E., Baker, V.R., Elachi, Charles, Saunders, R.S., and Wood, J.A., 1991, Magellan—Initial Analysis of Venus Surface Modification: Science, v. 252, p. 270–275.
Barsukov, V.L., Basilevsky, A.T., Burba, G.A., and 27 others, 1986, The geology and geomorphology of the Venus surface as revealed by the radar images obtained by Veneras 15 and 16: Journal of Geophysical Research, v. 91, p. 378–398.
Barsukov, V.L., Basilevsky, A.T., Kuz'min, R.O., and 8 others, 1984, Preliminary evidence on the geology of Venus from radar measurements by the Venera 15 and 16 probes: Geokhimia, v. 12, p. 1811–1820.
Basilevsky, A.T., 1986, The structure of the Ishtar Terra Central and Eastern parts and some tectonic problems of Venus, NASA TM-88508, *translation of* "Stroyeniye Tsentral'noy I Vostochnoy Chastey Zemli Ishtar I Nekotoryye Problemy Tektoniki Venery:" Geotektonika, v. 4, p. 42–53.
Basilevsky, A.T., and Head, J.W., 1995a, Global Stratigraphy of Venus—Analysis of a random sample of thirty-six test areas: Earth, Moon, and Planets, v. 66, p. 285–336.
Basilevsky, A.T., and Head, J.W., 1995b, Regional and global stratigraphy of Venus—A preliminary assessment and implications for the geological history of Venus: Planetary Space Science, v. 43, no. 12, p. 1523–1553.
Basilevsky, A.T., Head, J.W., Schaber G.G., and Strom R.G., 1997, The resurfacing history of Venus, *in* Bougher, S.W., Hunten, D.M., and Phillips, R.J., eds., Venus II: Tucson, University of Arizona Press, p. 1362.
Bender, K.C., Senske, D.A., and Greeley, Ronald, 2000, Geologic map of the Carson quadrangle (V–43), Venus: U.S. Geological Survey Investigation Series I–2620, scale ~1:5,000,000 [available on the World Wide Web at http://geopubs.wr.usgs.gov/i-map/i2620/].
Bindschadler, D.L., deCharon, Annette, Beratan, K.K., Smrekar, S.E., and Head, J.W., 1992a, Magellan observations of Alpha Regio—Implications for formation of complex ridged terrains on Venus: Journal of Geophysical Research, v. 97, E8, p. 13,563–13,577.
Bindschadler, D.L., and Head, J.W., 1991, Tessera terrain, Venus—Characterisation and models for origin and evolution: Journal of Geophysical Research, v. 96, p. 5889–5907.
Bindschadler, D.L., Schubert, Gerald, and Kaula, W.M., 1992b, Coldspots and hotspots—Global tectonics and mantle dynamics of Venus: Journal of Geophysical Research, v. 97, E8, p. 13,495–13,532.
Campbell, B.A., and Campbell, D.B., 1990, Western Eistla Regio—Radar properties of volcanic deposits: Geophysical Research Letters, v. 17, no. 9, p. 1353–1356.
Campbell, D.B., Head, J.W., Hine, A.A., Harmon, J.K., Senske, D.A., and Fisher, P.C., 1989, Styles of volcanism on Venus—New Arecibo high resolution radar data: Journal of Geophysical Research, v. 246, p. 373–377.
Campbell, D.B., Stacy, N.J.S., Newman, W.I., Arvidson, R.E., Jones, E.M., Musser, G.S., Roper, A.Y., and Schaller, C.J., 1992, Magellan observations of extended impact crater related features on the surface of Venus: Journal of Geophysical Research, v. 97, E10, p. 16,249–16,277.
Copp, D.L., 1997, Observations of stratigraphy and volcanism from Guinevere and Sedna Planitiae, Venus: University of London, unpublished Ph.D. dissertation, 308 p.
Copp, D.L., and Guest, J.E., 1995, Geology of the Sif and Gula quadrangle of Venus [abs.], *in* Lunar and Planetary Science Conference, 26th, March 1995: Houston, Tex., Lunar and Planetary Institute, p. 283–284.
Copp, D.L., Guest, J.E., and Stofan, E.R., 1997, Observations of selected coronae from Venusian quadrangles V–31 and V–19 [abs.], *in* Lunar and Planetary Science Conference, 27th, March 1996: Houston, Tex., Lunar and Planetary Institute, p. 259–260.
Copp, D.L., Guest, J.E., and Stofan, E.R., 1998, New insights into coronae formation—Mapping on Venus: Journal of Geophysical Research, v. 103, E8, p. 19,389–19,401.
Ford, J.P., Blom, R.G., Crisp, J.A., Elachi, Charles, Farr, T.G., Saunders, R.S., Theilig, E.E., Wall, S.D., and Yewell, S.B., 1989, Spaceborne radar observations—A guide for Magellan radar-image analysis: Pasadena, Calif., Jet Propulsion Laboratory Publication 89–41, 126 p.
Ford, P.G., and Pettengill, G.H., 1992, Venus topography and kilometer-scale slopes: Journal of Geophysical Research, v. 97, E8, p. 13,103–13,114.
Ford, J.P., Plaut, J.J., Weitz, C.M., Farr, T.G., Senske, D.A., Stofan, E.R., Michaels, Gregory, and Parker, T.J., 1993, Guide to Magellan image interpretation: Pasadena, Calif., Jet Propulsion Laboratory Publication 93–24, 148 p.
Gault, D.E., Quaide, W.L., and Oberbeck, V.R., 1968, Impact cratering mechanics and structures, *in* French, B.M., and Short, N.M., eds., Shock metamorphism of natural materials: Baltimore, Md., Mono Book Corp., p. 87–89.
Greeley, Ronald, Arvidson, R.E., Elachi, Charles, Geringer, M.A., Plaut, J.J., Saunders, R.S., Schubert, Gerald, Stofan, E.R., Thouvenot, E.J.P., Wall, S.D., and Weitz, C.M., 1992, Aeolian features on Venus—Preliminary Magellan results: Journal of Geophysical Research, v. 97, E8, p. 13,319–13,345.
Greeley, Ronald, Bender, K.C., and Senske, D.A., 1994, The Carson Quadrangle, Venus [abs.], *in* Lunar and Planetary Science Conference, 25th, March 1994: Houston, Tex., Lunar and Planetary Institute, p. 463–464.
Greeley, Ronald, and King, J.S., 1977, Volcanism of the Snake River Plain, Idaho—A comparative planetary geology guidebook: Washington, D.C., National Aeronautics and Space Administration CR–154621, 308 p.
Grimm, R.E., and Phillips, R.J., 1992, Anatomy of a Venusian hot spot—Geology, gravity, and mantle dynamics of Eistla Regio: Journal of Geophysical Research, v. 97, E10, p. 16,035–16,054.
Guest, J.E., Bulmer, M.H., Aubele, J.C., Beratan, K.K., Greeley, Ronald, Head, J.W., Michaels, Gregory, Weitz, C.M., and Wiles, C.R., 1992, Small volcanic edifices and volcanism in the plains of Venus: Journal of Geophysical Research, v. 97, E10, p. 15,949–15,966.
Guest, J.E., Lancaster, M.G., and Copp, D.L., 1995, Speculations on lava flow textures [abs.], *in* Lunar and Planetary Science Conference, 26th, March 1995: Houston, Tex., Lunar and Planetary Institute, p. 529–530.
Guest, J.E., and Murry, J.B., 1979, An analysis of hazard from Mount Etna volcano: Journal of Geological Society, v. 136, pt. 3, p. 347–354.
Guest, J.E., and Stofan, E.R., 2000, A new view of the stratigraphic history of Venus: Icarus, v. 139, p. 55–66.
Hansen, V.L., and Willis, J.J., 1996, Structural analysis of a sampling of Tesserae—Implications for Venus Geodynamics: Icarus, v. 123, p. 296–312.
Head, J.W., Campbell, D.B., Elachi, Charles, Guest, J.E., McKenzie, D.P., Saunders, R.S., Schaber, G.G., and Schubert, Gerald, 1991, Venus volcanism—Initial analysis from Magellan data: Science, v. 252, p. 276–288.
Janes, D.M., Squyres, S.W., Bindschadler, D.L., Baer, Gidon, Schubert, Gerald, Sharpton, V.L., and Stofan, E.R., 1992, Geophysical models for the formation and evolution of coronae on Venus: Journal of Geophysical Research, v. 97, E10, p. 16,055–16,067.
Lancaster, M.G., Guest, J.E., and Roberts, K.M., 1995, Great lava flow fields on Venus: Icarus, v. 118, 69–86.
McGill, G.E., 1993, Wrinkle ridges, stress domains, and kinematics of Venusian plains: Geophysical Research Letters, v. 20, p. 2407–2410.
McGill, G.E., 1994, Hotspot evolution and Venusian tectonic style: Journal of Geophysical Research, v. 99, E11, p. 23,149–23,161.
McKenzie, D.P., McKenzie, J.M., and Saunders, R.S., 1992, Dike emplacement on Venus and Earth: Geophysical Research Letters, v. 97, E10, p. 15,997–15,991.
Namiki, Noriyuki, and Solomon S.C., 1994, Impact crater densities on volcanoes and coronae on Venus—Implications for volcanic resurfacing: Science, v. 265, p. 929–933.
Pavri, B.E., Head J.W., Klose, K.B., and Wilson, Lionel, 1992, Steep-sided domes on Venus—Characteristics, geologic setting, and eruption conditions from Magellan data: Journal of Geophysical Research, v. 97, E8, p. 13,445–13,478.
Pettengill, G.H., Ford, P.G., Johnson, W.T.K., Raney, R.K., and Soderblom, L.A., 1991, Magellan—Radar performance and data products: Science, v. 252, p. 260–265.
Phillips, R.J., Arvidson, R.E., Boyce, J.M., Campbell, D.B., Guest, J.E., Schaber, G.G., and Soderblom, L.A., 1991, Impact craters on Venus—Initial analysis from Magellan: Science, v. 252, p. 288–297.
Phillips, R.J., Raubertas, R.F., Arvidson, R.E., Sarkar, I.C., Herrick, R.R., Izenberg, N.R., and Grimm, R.E., 1992, Impact craters and Venus resurfacing history: Journal of Geophysical Research, v. 97, E10, p. 15,923–15,948.
Plaut, J.J., Stofan, E.R., Crown, D.A., and Anderson, S.W., 1994, Topographic and surface roughness properties of steep-sided domes on Venus and Earth from radar remote sensing and field measurements [abs.], *in* Lunar and Planetary Science Conference, 25th, March 1994: Houston, Tex., Lunar and Planetary Institute, p. 1,091–1,092.
Price, M.H., and Suppe, John, 1994, Mean age of rifting and volcanism on Venus deduced from impact crater densities: Nature, v. 372, 756–759.
Price, M.H., Watson, J.G., Suppe, John, and Brankman, C.M., 1996, Dating volcanism and rifting on Venus using impact crater densities: Geophysical Research Letters, v. 101, p. 4657–4671.
Pronin, A.A., and Stofan, E.R., 1990, Coronae on Venus—Morphology and distribution: Icarus, v. 87, p. 452–474.
Roberts, K.M., and Head, J.W., 1993, Large-scale volcanism associated with coronae on Venus—Implications for formation and evolution: Geophysical Research Letters, v. 20, p. 1111–1114.
Ryan, M.P., Blevins, J.Y.K., Okamura, A.T., and Koyanagi, R.Y., 1983, Magma reservoir subsidence mechanics—Theoretical summary and application to Kilauea Volcano, Hawaii: Journal of Geophysical Research, v. 88, p. 4147–4181.
Sandwell, D.T., and Schubert, Gerald, 1992, Flexural ridges, trenches, and outer rises around coronae on Venus: Journal of Geophysical Research, v. 97, E8, p. 16,069–16,083.
Schaber, G.G., Strom, R.G., Moore, H.J., Soderblom, L.A., Kirk, R.L., Chadwick, D.J., Dawson, D.D., Gaddis, L.R., Boyce, J.M., and Russell, Joel, 1992, Geology and distribution of impact craters on Venus—What are they telling us?: Journal of Geophysical Research, v. 97, E8, p. 13,257–13,301.
Schultz, P.H., 1992, Atmospheric effects on ejecta emplacement and crater formation on Venus from Magellan: Journal of Geophysical Research, v. 97, E8, p. 16,183–16,249.
Senske, D.A., 1990, Geology of the Venus equatorial region from Pioneer Venus radar imaging: Earth, Moon, and Planets, v. 50/51, p. 305–328.
Senske, D.A., Head, J.W., Stofan, E.R., and Campbell, D.B., 1991, Geology and structure of Beta Regio, Venus—Results from Arecibo radar imaging: Geophysical Research Letters, v. 18, p. 1159–1162.
Senske, D.A., Schaber, G.G., and Stofan, E.R., 1992, Regional topographic rises on Venus—Geology of western Eistla Regio and comparison to Beta Regio and Atla Regio: Journal of Geophysical Research, v. 97, E8, p. 13,395–13,420.
Senske, D.A., and Stofan, E.R., 1993, Geologic mapping on Venus, *in* Ford, J.P., and others, eds., Guide to Magellan image interpretation: Pasadena, Calif., Jet Propulsion Laboratory Publication 93–24, 148 p.
Simkin, Tom, and Siebert, Lee, 1994, Volcanoes of the World (2d ed.): Tucson, Ariz., Geoscience Press Inc., 349 p.
Smrekar, S.E., 1994, Evidence for active hotspots on Venus from analysis of Magellan gravity data: Icarus, v. 112, p. 2–26.
Solomon, S.C., Smrekar, S.E., Bindschadler, D.L., Grimm, R.E., Kaula, W.M., McGill, G.E., Phillips, R.J., Saunders, R.S., Schubert, Gerald, Squyres, S.W., and Stofan, E.R., 1992, Venus tectonics—An overview of Magellan observations: Journal of Geophysical Research, v. 97, E8, p. 13,199–13,255.
Squyres, S.W., Janes, D.M., Baer, Gidon, Bindschadler, D.L., Schubert, Gerald, Sharpton, V.L., and Stofan, E.R., 1992, The morphology and evolution of coronae on Venus: Journal of Geophysical Research, v. 97, E8, p. 13,611–13,634.
Stofan, E.R., Bindschadler, D.L., Head, J.W., and Parmetier, E.M., 1991, Corona structures on Venus-Models of origin: Journal of Geophysical Research, v. 96, E11, p. 20,933–20,946.
Stofan, E.R., Guest, J.G., and Copp, D.L., 2001, Development of large volcanoes on Venus—Constraints from Sif, Gula, and Kunapipi Montes: Icarus, v. 152, p. 77–95.
Stofan, E.R., Hamilton, V.H., Janes, D.M., and Smrekar S.E., 1997, Coronae on Venus, morphology and origin, *in* Bougher, S.W., Hunten, D.M., and Phillips, R.J., eds., Venus II: Tucson, University of Arizona Press, 1362 p.
Stofan, E.R., Sharpton, V.L., Schubert, Gerard, Baer, Gidon, Bindschadler, D.L., Janes, D.M., and Squyres, S.W., 1992, Global distribution and characteristics of coronae and related features on Venus—Implications for origin and relation to mantle processes: Journal of Geophysical Research, v. 97, E8, p. 13,347–13,378.
Stofan, E.R., Smrekar, S.E., Bindschadler, D.L., and Senske, D.A., 1995, Large topographic rises on Venus—Implications for mantle upwelling: Journal of Geophysical Research, v. 100, E11, p. 23,317–23,327.
Tanaka, K.L., and 11 others, 1994, The Venus geologic mappers' handbook (2d ed.): U.S. Geological Survey Open-File Report 94–438.
Wilhelms, D.E., 1972, Geologic mapping of the second planet: U.S. Geological Survey Interagency Report, Astrogeology 55, p. 36.
Wilhelms, D.E., 1990, Geologic mapping, *in* Greeley, Ronald, and Batson, R.M., eds., Planetary mapping: New York, Cambridge University Press, p. 208–260.

ISBN 1-411-31761-0

Any use of trade, product, or firm names in this publication is for descriptive purposes only and does not imply endorsement by the U.S. Government
For sale by U.S. Geological Survey, Information Services, Box 25286, Federal Center, Denver, CO 80225, 1–888–ASK–USGS
Available at http://pubs.usgs.gov/sim/2007/2898

Printed on recycled paper